High-resolution bed level changes in relation to tidal and wave forcing on a narrow fringing macrotidal flat: Bridging intra-tidal, daily and seasonal sediment dynamics

Jean-Philippe Belliard[a,*], Alexandra Silinski[a,b], Dieter Meire[c], Gerasimos Kolokythas[c], Yaïr Levy[c], Alexander Van Braeckel[d], Tjeerd J. Bouma[e], Stijn Temmerman[a]

[a] University of Antwerp, Ecosystem Management Research Group, Universiteitsplein 1-c, B-2610 Antwerp, Belgium
[b] Göttingen University, Institute of Geography, Cartography, GIS and Remote Sensing Section, Goldschmidtstraße 5, 37077 Göttingen, Germany
[c] Flanders Hydraulics Research (FHR), Berchemlei 115, 2140 Antwerp, Belgium
[d] Research Institute for Nature and Forest (INBO), Havenlaan 88, 1000 Brussels, Belgium
[e] Royal Netherlands Institute for Sea Research (NIOZ), Korringaweg 7, 4401 NT Yerseke, Netherlands

ARTICLE INFO

ABSTRACT

Sediment dynamics in tidal flats, ranging from daily to seasonal timescales, are particularly relevant as they control key ecological and geomorphic processes that ultimately contribute to the long-term evolution of coastal and estuarine landscapes. Yet, insights into bed level changes, including the full range of relevant timescales from intra-tidal to daily and seasonal scales, are currently limited due to a lack of efficient methods to record high-resolution (< 1 day) data over the long-term (> 1 year). Accordingly, this contribution intends to improve our understanding on spatio-temporal patterns of long-term (> 1 year) high-resolution (daily) bed level dynamics in tidal flats in relation to the dominant hydrodynamic driving forces, namely tides and waves. Specifically, this study was conducted along two 200 m long cross-shore transects on an intertidal flat located in the macrotidal (> 5 m tidal range) Scheldt estuary, Belgium. Results showed that daily bed level changes at the low tidal flat (i.e. 4.10 m below mean high tide level) were dominated by tidal currents, with a strong fortnightly (or spring-neap) signature, whereas wave activity was of secondary importance. Conversely, bed level changes in the high tidal flat (i.e. 0.65 m below mean high tide level) were almost exclusively dominated by wave activity. Additionally, seasonal deposition–erosion cycles that superimposed on the daily bed level changes were associated with the seasonality of wind wave activity and benthic biology. Analysis of wave and current-induced bed shear stresses at the respective locations confirmed this spatial variability of tidal-dominated sediment dynamics at the low tidal flat versus wave-dominance at the high tidal flat, and comparison with local critical bed shear stresses for sediment motion also revealed differences in morphological impacts of the hydrodynamics between the two transects. These distinctive responses of bed level dynamics across the tidal flat can be partly explained by the spatially varying sediment properties across the tidal flat and may be further mediated, on a seasonal time scale, by the growth of the algal mat with its effect on stabilizing the sediment bed. In view of the large spatial and temporal variability of internal and external forcing revealed in this study, comprehensive and detailed field measurements are even more necessary to understand and predict long-term bed level dynamics and related ecological implications in tidal flats.

1. Introduction

Tidal flats are important wetland ecosystems common to many coasts and estuaries worldwide. They offer valuable ecosystem services such as the provision of rare and unique habitats for plants and benthic fauna (Paterson et al., 2009), including commercially important species for consumption (Barbier et al., 2011), as well as mitigation against coastal flood and erosion risks (Temmerman et al., 2013; Möller et al., 2014). Safeguarding these valuable ecosystem services is challenging, as tidal flats are highly dynamic ecosystems continuously changing due to erosion and sedimentation driven by tides and wind waves. Furthermore, tidal flat ecosystems are often impacted by anthropogenic

---

forcing on sediment dynamics, ranging from local (e.g. ship-induced waves) to global impacts (e.g. sea level rise).

In view of this context, there has been a wide scientific and economic interest in the complex sedimentary processes of tidal flats and their strong interactions with biota and anthropogenic factors across different timescales. While several studies have focused on the investigation of the long-term morphological response of coupled flat–marsh (and flat–mangrove) ecosystems to sea level changes, based on field data on decadal sediment dynamics (e.g. Carniello et al., 2009; Wang and Temmerman, 2013), studies based on field data that integrate daily to seasonal sediment dynamics are comparatively scarce. Specifically, high-resolution (~daily) bed level recordings in tidal flats over yearly periods have been long delayed by reason of a lack of appropriate measuring equipment and methods. Consequently, only a few recent studies have provided detailed quantification of high-resolution (daily and even higher resolutions) bed level dynamics, allowing to advance our understanding of sedimentary processes on daily to seasonal timescales in relation to forcing factors (hydrodynamics and sediment properties). Previous studies on high-resolution bed level dynamics were typically spanning over a few tidal cycles (e.g. Lee et al., 2004; Shi et al., 2014; Zhu et al., 2014) or a few months (e.g. Christiansen et al., 2006), while the few studies spanning over a year and more were instead limited in terms of the number of measurement stations (e.g. Christie et al., 1999; O'Brien et al., 2000; Deloffre et al., 2005; Verney et al., 2007). Alternatively, Yang et al. (2003), Hu et al. (2017) and Willemsen et al. (2018) provided long-term surveys of daily bed level recordings on a larger spatial scale, which brought up additional valuable insights into the spatio-temporal patterns of sediment dynamics and hydrodynamic forcing in tidal flats. Nevertheless, two of the latter studies did not involve long-term high-resolution measurements of tidal and wave forcing in situ; hydrodynamic data were either derived by numerical modelling (Hu et al., 2017) or collected at nearby tidal gauges and wave measurement stations (Yang et al., 2003).

The majority of the previous studies dealt with relatively wide and gently sloping tidal flats, often located within large coastal embayments and near estuary mouths, and which have been the main focus of reviews on tidal flat geomorphology (see e.g. Amos, 1995; Pethick, 1996; Dyer et al., 2000a; Gao, 2009). However, tidal flats can also be found in more sheltered areas further upstream, mostly in estuaries subject to a macrotidal regime. They generally present a narrower and steeper topographic profile, often being convex-up, which has been shown to be associated with tidal dominance and sediment accretion (Pethick, 1996). Yet, observations of wave-dominated tidal flats in inner parts of macrotidal estuaries also exist (e.g. Verney et al., 2007), despite wave dominance usually favors wider, flatter and concave-up topographic profiles (Pethick, 1996; Bearman et al., 2010). In inner tidal estuaries, ship-induced waves can indeed highly contribute to the overall wave activity and cause strong impacts on narrow fringing tidal flats, since their limited widths cannot attenuate waves efficiently and their relatively steep slopes could instead maintain or even increase wave heights by shoaling (le Hir et al., 2000). Engineering works, such as historical land reclamation and shoreline hard defenses, which are likely to be present in inner urbanized tidal estuaries, constitute additional anthropogenic forcing providing further constraints on the morphology of tidal flats (Friedrichs, 2011). The constrained width of narrow fringing tidal flats may also, to some extent, be imposed by the antecedent geology as the width of paleo-river valleys typically decreases upstream. This combination of several independent forcing results in complex sediment dynamic and morphodynamic responses of inner fringing tidal flats which presently are still not fully understood.

In the present contribution, we intend to further build on these previous studies by analyzing in situ comprehensive measurements of tidal hydrodynamics, wind and wave climates, suspended sediment concentrations, sedimentary properties and bed level changes at high-resolution (daily) over a period of more than a year in several locations in a tidal flat located in the inner Scheldt estuary, Belgium. The study area is subject to a macrotidal regime as well as frequent ship-induced waves. Therefore, elucidating the dominant hydrodynamic forcing on sediment dynamics in this site, and how this depends on the location along cross-shore transects from low to high intertidal zone, is relevant for the understanding of sediment dynamics in narrow estuarine-fringing tidal flats in general. Indeed, while it is well-acknowledged that sedimentary processes in micro- to meso-tidal flats are typically dominated by waves, as demonstrated by numerous studies on various estuarine sites (see Green and Coco, 2014 for a review), the morphological significance of a single hydrodynamic forcing is rare in macro-tidal flats. Sedimentary processes may be dominated by either (or both) tides and waves depending on the actual location in the tidal flat as well as on the time scale of interest (e.g. Christie et al., 1999; O'Brien et al., 2000).

Accordingly, in the present study, we intend to (i) provide additional insights into the complex spatio-temporal patterns of high-resolution bed level dynamics, spanning intra-tidal, daily to seasonal timescales, (ii) unravel the relative contributions of tides, waves and induced bed shear stresses in controlling these high-resolution sediment dynamics, and (iii) demonstrate how the dominant forcing factors (tides, waves) spatially depend on the location along cross-shore transects from the low to high intertidal zone in a macrotidal estuary.

2. Materials and methods

2.1. Study site

Field work was conducted at the 'Galgeschoor' (51°19′1.60″ N, 4°17′53.43″ E), a nature reserve of tidal marshes and flats located within the brackish zone of the Scheldt estuary, Belgium (Fig. 1), 65 km upstream from the estuary mouth.

The Galgeschoor is an estuarine fringing tidal wetland with an along-shore length of approximately 3.5 km and a maximum cross-shore length of 300 m. The tidal marsh is found at elevations near or above the local mean high water level and is dominated by *Phragmites australis*. At the tidal marsh – flat transition, an almost continuous cliff is present, with heights of up to 50 cm locally. The tidal flat extends further seaward from the marsh edge where a riprap first covers an elevation gradient of maximum 2 m locally to stabilize a steep slope, followed by a more gentle slope all the way down to the estuarine channel (Fig. 2).

The hydrodynamic conditions in the study area are primarily characterized by a semi-diurnal macrotidal regime. Recorded water levels at the nearby Liefkenshoek tidal gauge (see Fig. 1) during the field campaign showed a mean tidal range of 5.2 m, and mean spring and neap tidal ranges of 6.1 and 4.1 m, respectively. Annually averaged freshwater discharge from the river Scheldt typically varies from 100 to 200 $m^3 s^{-1}$ in the area (Maris and Meire, 2016). The wave climate is characterized by fetch-limited wind waves with a rather short to moderate wind fetch of the dominant south south-westerly winds (< 2 km). On the other hand, the Galgeschoor experiences frequent ship-induced waves as being located right within the area of the port of Antwerp where the shipping channel passes close to the tidal flat (see Fig. 1; an average of 1500 ship passages per week were recorded during the field campaign). With regard to water quality, averaged surface suspended sediment concentration (SSC) from 2009 to 2017 at Liefkenshoek is $77.7 \pm 53.5 \, mg \, L^{-1}$ while averaged bottom SSC is $287.4 \, mg \, L^{-1}$. Furthermore, averaged salinity at Liefkenshoek is 8.3 ± 3.9 ppt during that period, reaching a maximum 17.4 ppt in summer and a minimum 0.8 ppt in winter (Maris and Meire, 2016).

2.2. Field measurements

Two cross-shore measuring transects were established on the tidal flat: (i) a southern transect, called hereafter S, and (ii) a northern transect, called hereafter N (see Fig. 1). The topographic profiles of the
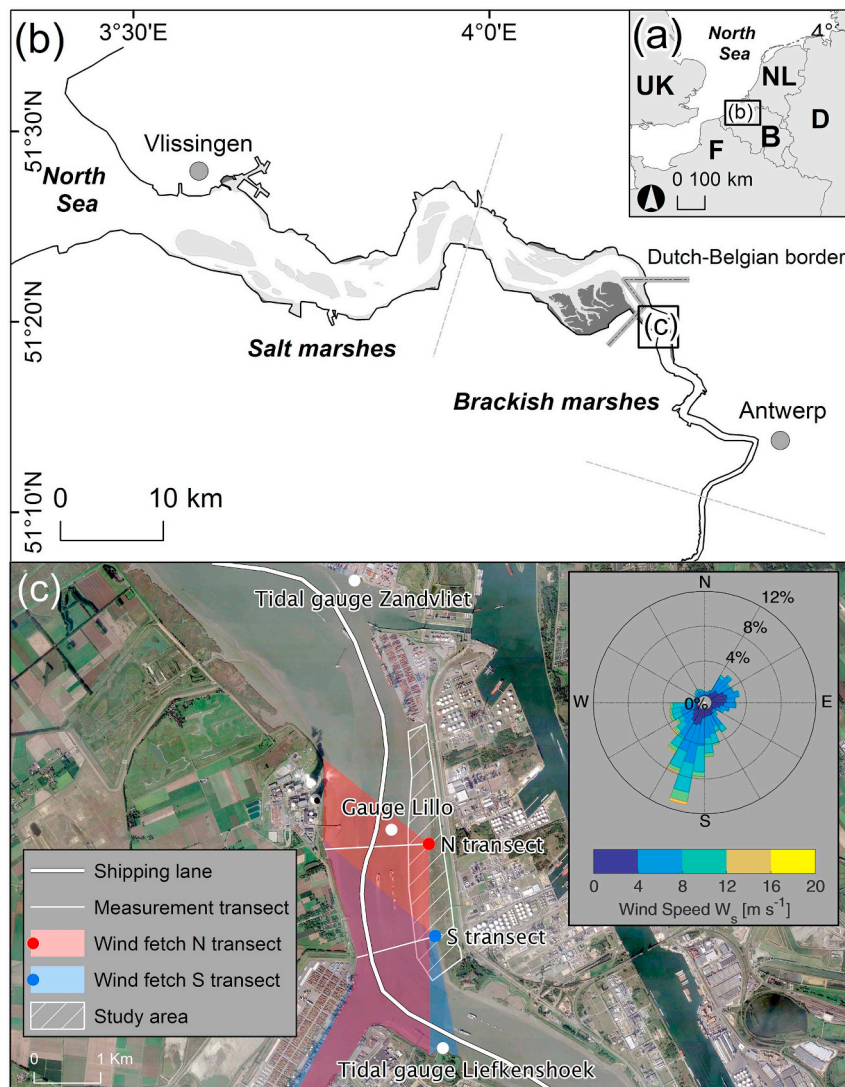
Fig. 1. Overview of the location of the Scheldt estuary (a) within Europe, (b) over the stretch from Antwerp to the North Sea and (c) of the study area. Locations of the Galgeschoor (hatched area), the northern (N) and southern (S) measurement transects (white lines), the gauge stations used for additional field data collection and the shipping lane are indicated. Wind rose diagram from the Zandvliet station showing the wind conditions that occurred during the long-term field campaign and corresponding wind fetch for the main wind directions per measurement transect are also displayed.

two transects are depicted in Fig. 2. At each transect, two measurement stations representative of the respective high and low tidal flat conditions were selected (labelled as H and L, respectively). It is worth to note that these high and low stations are not completely in natural communication with each other because of the presence of the riprap in between. At the start of the field campaign, the elevations of the high and low stations of the southern transect (SH and SL) were 4.69 m and 1.11 m relative to TAW (i.e., the Belgian ordnance datum; 0 m TAW ≈ −2.0 m amsl), respectively. The initial elevations of the high and low stations of the northern transect (NH and NL) were 5.00 m TAW and 0.57 m TAW, respectively.

2.2.1. Long-term field campaign

A long-term (18 months) field campaign started on October 27, 2015 during which topographic, sedimentological and hydrodynamic measurements were conducted. Bed level changes were monitored daily using Sediment Elevation Dynamics sensors (SED sensors; Hu et al., 2015) deployed simultaneously at the four measurement stations. These newly-developed instruments consist of single arrays of light sensitive cells that measure light intensity returned in a voltage output from which an actual bed level can be determined. These light sensitivity

cells are packed into a transparent tube and enclosed together with data loggers and batteries into a stainless steel case which is inserted vertically into the bed. SED sensors can only measure reliably when light intensity is high, that is during daytime and emerged conditions, such that the interval between two consecutive measurements can be more than one tidal cycle. For most of the time, SED sensors provided at least one measurement per day (i.e. approximately daily temporal resolution), with a vertical accuracy of ~2 mm (Hu et al., 2015). For backup and validation purposes, SED-based bed level monitoring was supplemented with monthly bed level measurements using two other well-established methods: (i) Sedimentation Erosion Bars (SEB), with a vertical accuracy of 1.5 mm (Nolte et al., 2013), and (ii) using a Real Time Kinematic Global Positioning System (RTK-GPS), with a vertical accuracy of 1 cm, at every measurement station. Additionally, during these monthly topographical surveys, surface sediments of the upper 2 cm were sampled for subsequent sedimentological analysis. To monitor water levels and wave characteristics, absolute pressure was measured using two PDCR 1830 pressure transducers (General Electric sensing) deployed at SH and SL during the long-term campaign. These pressure sensors were mounted on a stainless-steel plate placed horizontally above the bed, with the actual sensor located 7.5 cm above the
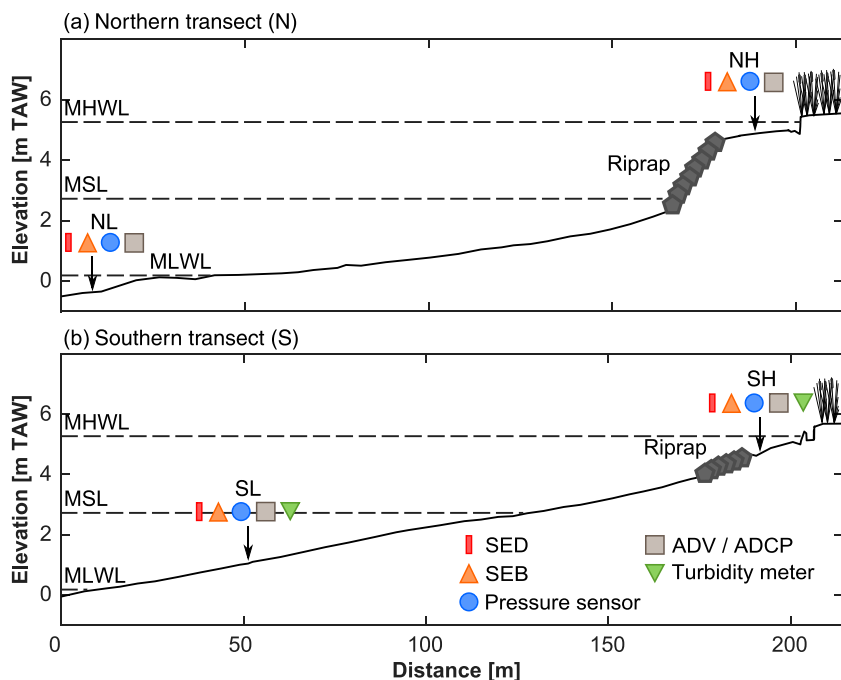
Fig. 2. Topographic profiles of (a) the northern (N) and (b) southern (S) measurement transects. These profiles were processed using elevation data recorded with the help of a RTK GPS on November 3, 2015 (at the start of the field campaign). Distances are landward (from the estuarine channel toward the marsh). Locations of measurement stations with corresponding instrumentation are also indicated for both transects. Note that the pressure sensors at the N transect, ADVs/ADCPs and turbidity meters at both N and S transects were only deployed during the intensive campaign.

sediment surface, and were connected via a cable to a PVC shell containing a data logger and batteries. Absolute pressure was recorded at a sampling rate of 16 Hz continuously.

2.2.2. Intensive field campaign

Complementary to the long-term 18-month field campaign, an overlapping intensive 6-week field campaign took place starting on October 27, 2016, with the same field experimental set-up but with several additional instruments. Tidal and wave-driven water level variations were additionally recorded at NH and NL using two OSSI-010-003C pressure transducers (Ocean Sensor Systems, Inc.). These self-logging pressure sensors were inserted into the bed just below the sediment surface looking upward. Absolute pressure was recorded at a sampling rate of 20 Hz continuously. Near-bed 3D current velocities were measured using two acoustic Doppler velocimeters (ADV, Nortek vectors) deployed at NH and SH. The ADVs were fixed on a rigid aluminum frame, with the sensor probes oriented horizontally at 15 cm above the bed. To allow long autonomous deployments and full tidal cycle recordings, velocities were recorded in bursts at a sampling rate of 1 Hz for 4 h 45 min with a time interval between bursts of 8 h. Current velocity profile was measured using two acoustic Doppler current profilers (ADCP, Nortek Aquadopp) deployed at NL and SL. The ADCPs were inserted into the bed just below the sediment surface with the sensors looking upward. Current velocity profile was recorded every 5 min continuously. Turbidity was measured at SH and SL yet using different apparatus. At SH, turbidity was measured by an Optical Back-Scatter (OBS; Campbell Scientific) 3+ sensor logged by the ADV on one of its analogue channels, thus with similar sampling rate, burst duration and interval, and measurement height settings. Conversely, at SL, turbidity was measured using an YSI 6600 Sonde (YSI co.) equipped with an YSI 6136 optical sensor. The instrument was fixed inside a cage attached to a wooden pole with the sensor probe looking downward at a height of 30 cm above the sediment surface. Turbidity was recorded every 30 s continuously.

2.3. Additional field data collection

Low and high tidal water levels recorded at the Liefkenshoek tidal gauge located in the estuarine channel near the study site (see Fig. 1)

were collected during the long-term campaign. Wind speed (W_s) and direction (W_{dir}) recorded at the nearby Zandvliet weather station at a height of 10 m above the ground as well as atmospheric pressure recorded at the Melsele weather station were also collected during the long-term campaign. SSC was obtained from validated turbidity measured at the Lillo measurement pole located in the estuarine channel just offshore of the tidal flats of Galgeschoor. Turbidity was measured by two Aanderaa Seaguard turbidity sensors (Aanderaa co.) which were mounted on the measurement pole at 1 m and 3.75 m above the channel bed, respectively. Lastly, Automatic Identification System (AIS) data were requested from the Vessel Traffic Services in order to collect information about ship position, type, course, speed, etc. for every ship crossing in the study area during the intensive campaign. Table 1 provides a summary of the variables/parameters measured or collected during the entire field campaign (both long-term and intensive).

2.4. Data processing and derived variables

2.4.1. Bed levels

As the measuring window of SED sensors is during daytime emerged conditions, SED output signals recorded during nighttime were excluded and the remaining signals were constrained within ± 1 h of low water time. The actual bed level was then determined by identifying the cell number at which the transition point occurred between the low and high voltage values returned by the belowground and aboveground cells, respectively, and multiplying it by the cell length (2 mm). Sometimes, manual filtering was necessary, especially when water was still draining after the receding tide, which could have otherwise led to spurious bed level determination. SED-derived bed levels were then compared with SEB-derived bed levels.

2.4.2. Sediment characteristics

Monthly collected sediment samples were weighted and oven dried at 70 °C for 48 h until reaching a constant weight to subsequently determine sediment textural composition and grain size (using a Laser Diffraction Particle Size Analyzer LDPSA– COULTERN LS13320) and organic matter content (determined by loss on ignition – LOI).

Table 1

Summary of variables/parameters measured in the field or collected (in italic) during the field campaign.

Parameter	Location	Method	Measurement period	Temporal resolution
Bed level	N/S	SED	Nov. 2015–May 2017	1 day
	N/S	SEB	Nov. 2015–May 2017	1 month
	N/S	RTK–GPS	Nov. 2015–May 2017	1 month
Water level	S	Pressure transducer (PDCR 1830)	Nov. 2015–Feb. 2017	16 Hz
	N	Pressure transducer (OSSI-010-003C)	Nov. 2016 (Intensive campaign)	20 Hz
	Liefkenshoek	*Radar (OTT-RLS)*	*Nov. 2015–May 2017*	*1 min*
Waves	S	Pressure transducer (PDCR 1830)	Nov. 2015–Feb. 2017	16 Hz
	N	Pressure transducer (OSSI-010-003C)	Nov. 2016 (Intensive campaign)	20 Hz
Flow velocity	NH/SH	ADV (Nortek Vector)	Nov. 2016 (Intensive campaign)	1 Hz
	NL/SL	ADCP (Nortek Aquadopp)	Nov. 2016 (Intensive campaign)	5 min
Turbidity	SH	OBS 3 +	Nov. 2016 (Intensive campaign)	1 Hz
	SL	YSI 6136	Nov. 2016 (Intensive campaign)	30 s.
Bed grain size	N/S	LDPSA	Nov. 2015–Jan. 2017	1 month
SSC[a]	*Lillo*	*Aanderaa Seaguard*	*Nov. 2015–Apr. 2017*	*10 min*
AIS[b] (*ship data*)	*Galgeschoor area*		*Nov. 2016 (Intensive campaign)*	*Ship dependent*
Wind[c]	*Zandvliet*		*Nov. 2015–Jan. 2017*	*1 min*
Atmospheric pressure	*Melsele*		*Nov. 2015–Feb. 2017*	*15 min*

[a] Data obtained from the Hydraulic Information Centre (HIC) – Flanders Hydraulics Research, Antwerp, Belgium (06/2017).
[b] Data obtained from the Scheldt Radar Keten (SRK).
[c] Data obtained from Antwerp Port Authority.

2.4.3. Hydrodynamics

Absolute pressure was first corrected for atmospheric pressure recorded at the Melsele weather station, and then converted to meters of water. Resulting water levels were subsequently corrected for depth-dependent pressure attenuation based on the linear wave theory using a maximum correction factor equal to 6.7, following the findings of Vanlierde et al. (2011). Then, low water level records at the Liefkenshoek tidal gauge were used to divide water levels per tidal cycle from which the corresponding energy spectrum was reconstructed. A low pass filter with a cutoff frequency of 0.002 Hz was then applied in the energy spectrum to extract the tidal signal component and to obtain the time series of surface wave fluctuations. Zero-downcrossing method was then applied to determine individual waves for which wave parameters including wave height (H), period (T), length (λ) and steepness (H/λ) were calculated. The applied method foresees the detection of outliers, i.e. samples with heights that differed by more than four standard deviations from a moving median of a window of 25 samples were subsequently removed. Moreover, significant and maximum wave heights (H_s and H_{max} respectively) and periods (T_s and T_{max} respectively) were calculated over semi-diurnal tidal cycles.

Estimates of bed shear stress induced by waves were determined from a wave-by-wave (as opposed to burst averaged) approach, i.e. using the wave parameters calculated for individual waves. Applying a quadratic friction law, the wave-induced bed shear stress τ_w (N m^{-2}) reads:

$$\tau_w = \frac{1}{2}\rho f_w U_w^2 \tag{1}$$

where ρ (kg m^{-3}) is the water density, U_w (m s^{-1}) is the amplitude of the wave orbital velocity and f_w (−) is the wave friction factor estimated as (Fredsøe and Deigaard, 1992):

$$f_w = 0.04\left(\frac{A_w}{k_N}\right)^{-0.25} \tag{2}$$

which depends, for a turbulent hydraulic regime, on the semi-orbital

wave excursion $A_w = U_w T/2\pi$ (m) relative to the bed roughness length $k_N = 2.5d_{50}$ (m) evaluated here as a grain roughness with d_{50} being the median sediment diameter. τ_w is therefore defined as a skin friction, which is the component of the bed shear stress acting on the sediment grains. For regular (monochromatic) waves, U_w can be evaluated with the linear wave theory as follows:

$$U_w = \frac{\pi H}{T \sinh(kh)} \tag{3}$$

where $k = 2\pi/\lambda$ (m^{-1}) is the wave number and h (m) is the local water depth.

Estimates of bed shear stress induced by tidal currents were determined from the current velocity measurements, previously filtered out from noise level. Specifically, ADV-derived velocity measurements were processed by removing all raw ADV data with signal-to-noise ratio (SNR) < 5 dB and beam correlation < 70%. Using the ADV-derived velocity measurements, the current-induced bed shear stress τ_c (N m^{-2}) was calculated as follows:

$$\tau_c = \rho u_*^2 \tag{4}$$

where u_* (m s^{-1}) is the friction velocity, which for steady currents can be expressed as:

$$u_* = \kappa U(z)/\ln(z/z_0) \tag{5}$$

where $\kappa = 0.40$ (−) is the von Karman's constant, U (m s^{-1}) is the magnitude of the horizontal components of current velocity at height z above the bed (i.e. ADV height) and $z_0 = k_N/30$ such that τ_c becomes a skin friction, similar to τ_w. Likewise, the current-induced skin-friction τ_c (N m^{-2}) utilizing the ADCP-derived velocity measurements was expressed as a quadratic friction law, yielding:

$$\tau_c = \frac{1}{8}\rho f_c U^2 \tag{6}$$

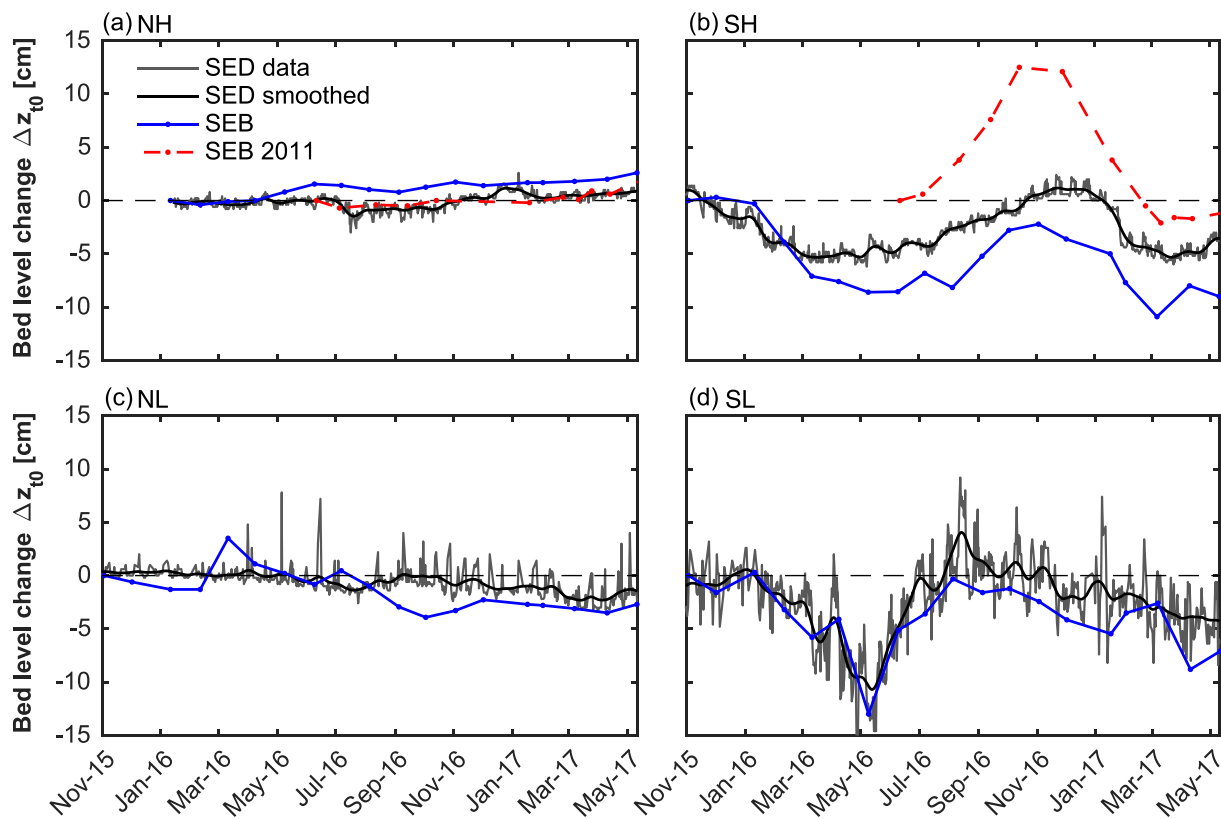where f_c (−) is the friction factor of Darcy-Weisbach which is evaluated as:

Fig. 3. Temporal evolution of SED-derived (grey lines) and monthly SEB-derived (blue dotted lines) bed level changes relative to t_0 (Δz_{t0}) recorded at the (a) northern high (NH), (b) southern high (SH), (c) northern low (NL) and (d) southern low (SL) tidal flat measurement stations during the long-term campaign (i.e. from October 29, 2015 to May 11, 2017). The absence of bed level data at NH at the beginning of the field campaign was due to a technical failure of the corresponding SED sensor. Every SED-derived bed level change time series was smoothed out using a weighted moving average with a Gaussian window of 1 month (black lines). Time evolution of monthly SEB-derived bed level changes monitored at NH and SH as part of a previous field campaign in 2011 (red dotted lines) are displayed for comparison. For all data series, negative values represent net erosion and positive values represent net deposition. Note that the corresponding SEB plot and SED sensor were deployed at the same exact location at site SL, while at the other sites, the respective SEB plot and SED sensor were placed a few meters apart. (For interpretation of the references to colour in this figure legend, the reader is referred to the web version of this article.)

$$f_c = 0.24 \left[\log \left(\frac{12h}{k_N} \right) \right]^{-2} \tag{7}$$

with U (m s^{-1}) is the depth-averaged flow velocity.

To estimate sediment entrainment, τ_w and τ_c are compared with the local critical bed shear stress for initiation of sediment motion τ_{cr} which can be expressed as a function of the Shields parameter θ_{cr} ($-$) as follows:

$$\tau_{cr} = \theta_{cr} (\rho_s - \rho) g d_{50} \tag{8}$$

with ρ_s (kg m^{-3}) is the sediment diameter and g (m s^{-2}) is the gravitational acceleration. Using the Shields' curve, Soulsby and Whitehouse (1997) proposed an algebraic relationship linking θ_{cr} with the sediment diameter, given by:

$$\theta_{cr} = \frac{0.30}{1 + 1.2 D^*} + 0.055 [1 - \exp(-0.020 D^*)] \tag{9}$$

where D^* ($-$) is the dimensionless sediment diameter, defined as:

$$D^* = \left[\frac{g(s - 1)}{\nu^2} \right]^{1/3} d_{50} \tag{10}$$

with $s = \rho_s / \rho$ ($-$) is the relative sediment density and ν (m^2 s^{-1}) is the kinematic viscosity.

2.5. Time series and statistical analyses

Bed level changes were expressed as relative to the first

measurement t_0 (hereinafter denoted as Δz_{t0}). To better visualize the presence of trends or any other long-term temporal components, the original bed level change data were smoothed using a weighted moving average with a Gaussian window of 1 month. To analyze and characterize short-term (daily) fluctuations, bed level change data were first detrended by subtracting the smoothed series to the original one. A Lomb-Scargle transform (Scargle, 1982; Press et al., 1992) was then performed on the detrended bed level change time series to identify the presence of short-term periodicities. Unlike classical auto-spectral Fourier transform, this method offers the advantage to work directly on unevenly spaced data, in line with the approximate daily temporal resolution provided by the SED sensors. Additionally, the presence of short-term periodicities was illustrated by computing the auto-correlation of the detrended bed level change time series for which a shape-preserving piecewise interpolation on an evenly spaced time vector was performed. Moreover, to map changes in the time-frequency domain, a 1-D continuous wavelet transform (CWT) was computed using a Morlet mother wavelet (with wave number $\omega_0 = 6$).

In addition to time series analysis, inferential and bivariate statistical analyses were carried out on the data set. More specifically, statistical differences in bed level changes and sediment characteristics between the four measurement stations were assessed using one-way ANOVA or the equivalent Kruskal Wallis non parametric test when assumptions of data normality and variance homogeneity were not met, followed by multiple pairwise comparisons. Relations between daily bed level changes and hydrodynamic forcing and SSC were explored by linear correlation analysis using Spearman's rank correlation coefficient

r_s because most data were not normally distributed. For a matter of data consistency, the variables tested for correlation against bed level changes were recast by taking maximum values between consecutive bed level measurements. Data normality was assessed using Anderson–Darling test (Anderson and Darling, 1952). All time series and statistical methods were carried out with a 95% confidence interval. Data processing and subsequent time series and statistical analyses were performed using MATLAB R2016a.

3. Results

3.1. Long-term daily and seasonal patterns of bed level dynamics

A good agreement is found between records of bed level changes Δz_{t0} derived from the SED and SEB measurements at the four tidal flat measurement stations during the long-term campaign, as shown in Fig. 3. Both SED and SEB-derived bed level changes showed a seasonal pattern at SH and SL over the long-term, whereby negative bed level changes, i.e. erosion, occurred from autumn to spring, followed by positive bed level changes, i.e. deposition, from spring to autumn, with slight time shifts depending on the considered station. In contrast, no seasonal pattern was observed at NH and NL, and bed level changes were in general less pronounced. Although interpretations of the long-term seasonality of bed level changes should be taken with great care due to the relatively short length of the time series, observed SEB-derived records of bed level changes resulting from a previous field campaign performed in 2010–2011 also show the presence of such a seasonality at site SH, and absence of such a seasonal pattern at NH.

The SED measurements also show that short-term (daily) fluctuations of bed level changes are superimposed upon the long-term seasonal pattern (Fig. 3). These daily fluctuations are of higher magnitude at the low (NL and SL) than high (NH and SH) stations. In line with this observation, Fig. 4 displays the time series of the median sediment diameter d_{50} of the surface sediments collected monthly during the long-term campaign at the four stations. Stations that depict high daily bed level fluctuations also portray the coarsest surface sediments. In particular, d_{50} at SL clearly stands out from the three other stations (Kruskal Wallis, $\chi^2 59,3 = 40.51$; $p < 0.001$). Similar pattern can be observed when looking at the textural composition of the surface sediments at the considered stations (Fig. S1 in Supporting information). Indeed, the mud fraction (clay and silt fractions combined) accounted for > 50% of the total sediment composition at NH, SH and NL throughout the entire long-term campaign, suggesting a higher cohesion between sediment grains at these locations than at SL where the sediment composition was significantly different (ANOVA,

$F_{59,3} = 49.87$; $p < 0.001$), with sand representing the dominant sediment fraction.

To further characterize these daily bed level fluctuations, the Lomb-Scargle power spectral density was computed for the detrended bed level changes recorded at the four measurement stations (Fig. 5). A highly significant frequency peak, corresponding to a fortnightly period (i.e. $T{\sim}14.7$ days), occurred at the low stations SL and NL (the latter to a lesser extent). This observed fortnightly periodicity suggests the presence of a spring–neap tidal signature in the daily fluctuations of bed level changes at the low tidal flat. Comparatively, the same primary frequency peak in the daily bed level changes was much less pronounced at the high tidal flat stations SH and NH. The presence of this fortnightly periodicity at the low tidal flat can be further illustrated by computing the correlogram of the bed level changes, after detrending and interpolation on evenly spaced time vectors (Fig. S2). In analogy with the Lomb-Scargle power spectral density, the fortnightly periodic pattern is clearly discernible at the low tidal flat, especially at SL, while it is weaker at the high tidal flat, notably at NH where the correlation starts to drop below the 95% confidence bounds after lag = 90 days.

To examine the temporal evolution of the strength of the observed fortnightly periodicity present at the low tidal flat, Fig. 6 shows the continuous wavelet power spectrum performed on the corresponding detrended and interpolated bed level changes. The power of this fortnightly periodicity at SL varies in time with the occurrence of peaks in March – June 2016, August – September 2016 and January – February 2017, as illustrated by the respective clusters of high wavelet power. This fortnightly periodicity also depicts a time variability at NL, yet with a much lower power globally and with peak periods not necessarily coinciding with those observed at SL.

In the next section we will then examine which external forcing factor(s) can explain the observed short-term (daily) fluctuations in bed level changes.

3.2. Relations of daily bed level dynamics to external forcing

3.2.1. General time series

Dominant wind directions W_{dir} during the long-term campaign ranged from southerly to southwesterly winds (Fig. 7a; see also Fig. 1), with 69% of all recorded W_{dir} belonging to the south-west quadrant. While no seasonal pattern arose in W_{dir} during the long-term campaign, a seasonality in wind speed W_s was observed, with higher W_s during the winter months and lower W_s during the spring and summer months. Stormy conditions (light blue-shaded areas), defined by the 90th percentile threshold of W_s and here taken as 11.2 m s^{-1}, mostly occurred in winter, coinciding with the dominant W_{dir}.
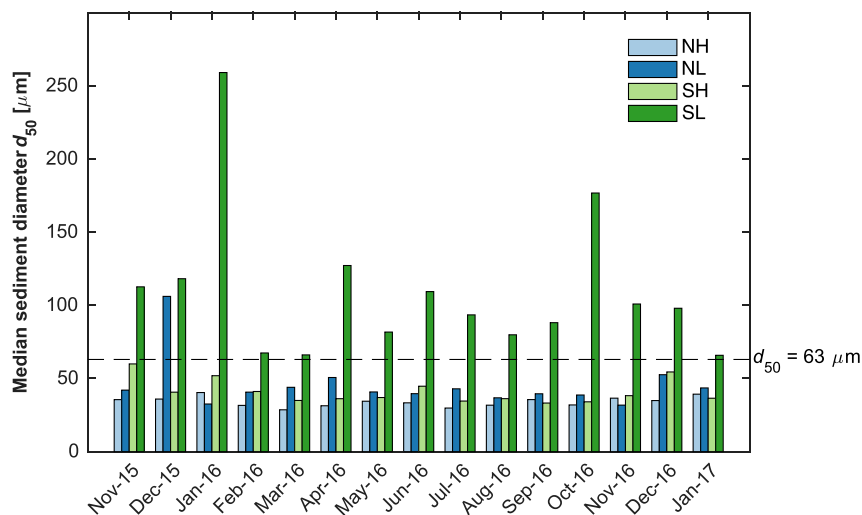

Fig. 4. Temporal evolution of the median sediment diameter d_{50} of sediment samples collected monthly at the northern high (NH), northern low (NL), southern high (SH) and southern low (SL) tidal flat measurement stations. Sediment samples were collected up to a depth of 2 cm from the surface. Sediment grain size was determined using LDPSA. The dash line $d_{50} = 63$ μm defines the limit between cohesive and non-cohesive sediments based on the grain size distribution.
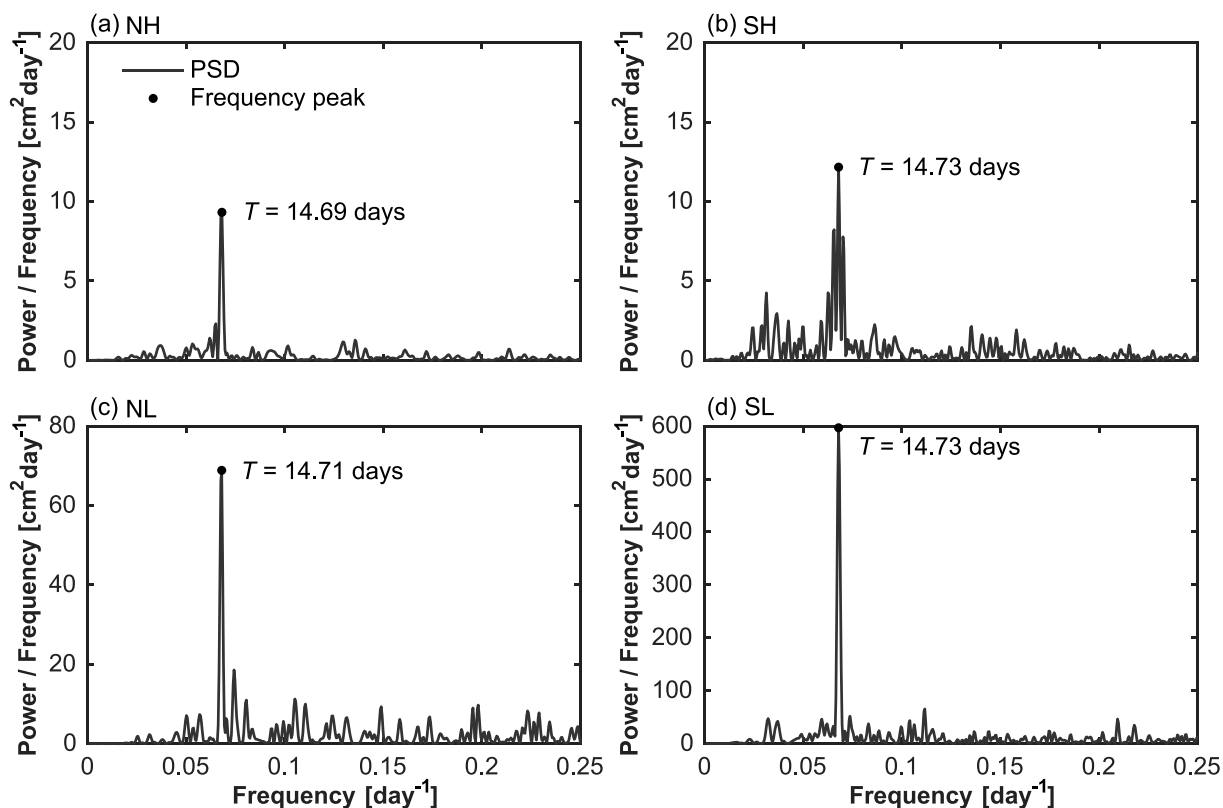
Fig. 5. Lomb-Scargle power spectral density (PSD) of the detrended bed level changes recorded at the (a) northern high (NH), (b) southern high (SH), (c) northern low (NL) and (d) southern low (SL) tidal flat measurement stations during the long-term campaign (i.e. from October 29, 2015 to May 11, 2017). Main frequency peaks occurred precisely at (a) $f = 0.068$ days^{-1} ($T = 14.74$ days) for NH, (b) $f = 0.068$ days^{-1} ($T = 14.73$ days) for SH, (c) $f = 0.067$ days^{-1} ($T = 14.76$ days) for NL and (d) $f = 0.068$ days^{-1} ($T = 14.73$ days) for SL.
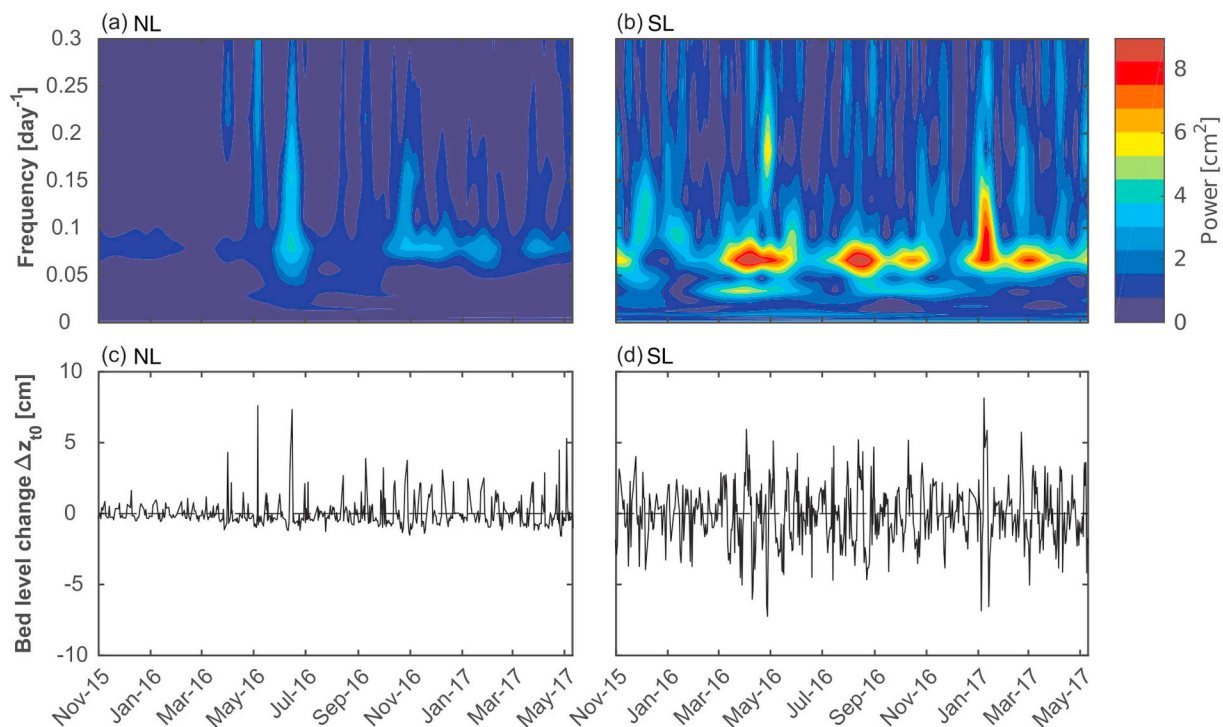

Fig. 6. Wavelet power spectrum of the detrended bed level changes recorded at the (a) northern low (NL) and (b) southern low (SL) tidal flat measurement stations during the long-term campaign (i.e. from October 29, 2015 to May 11, 2017), and supplemented with corresponding time series of detrended bed level changes at (c) NL and (d) SL.
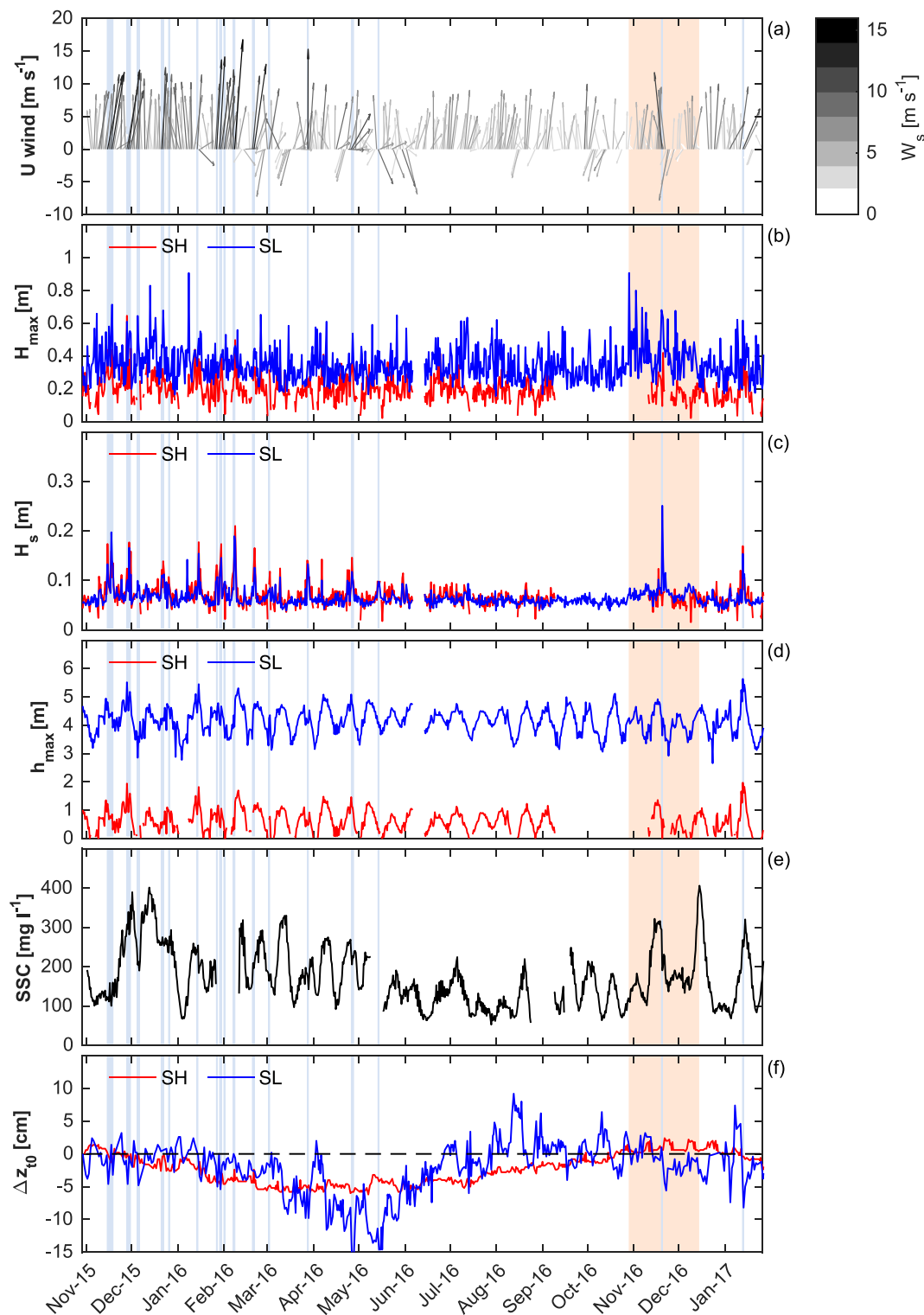
Fig. 7. Temporal evolution of (a) daily-averaged wind speed W_s and direction W_{dir}, (b) tidally-maximum wave heights H_{max}, (c) tidally-significant wave height H_s, (d) water depth at high tide h_{max}, (e) tidally-averaged SSC and (f) bed level changes Δz_{t0} from October 29, 2015 to January 17, 2017 (for clarity purpose all time series were displayed until January 17, 2017 corresponding to the end of the wind measurement records; see Table 1). Panels b, c, d and f are further differentiated by measurements performed at the southern high (SH, red lines) and low (SL, blue lines) tidal flat stations. Note that the pressure sensor deployed at SH experienced a technical failure which did not allow obtaining measurements from September 11 to November 09, 2016. Additionally, the two pressure sensors deployed at SH and SL were removed from the field from June 06 to June 13, 2016 for cleaning and maintenance purposes. SSC displayed in panel e was determined on the basis of turbidity measured by the upper Anderaa Seaguard sensor at the Lillo measurement pole. SSC was derived using a SSC – turbidity linear relationship drawn up following calibration campaigns that took place at Lillo where a large number of samples were taken, on which SSC was determined and related to turbidity recorded at the same time. Only SSC data based on validated (quality controlled) turbidity values are displayed. Light blue-shaded areas indicate stormy conditions, as defined by the 90th percentile of wind speed, here taken as $11.2\,\mathrm{m\,s^{-1}}$. The light beige-shaded area delineates the period where the intensive campaign took place. (For interpretation of the references to colour in this figure legend, the reader is referred to the web version of this article.)

Globally, wave climate measured at SH and SL showed a seasonal trend similar to wind climate, where higher H_{max} and H_s occurred during winter, and lower H_{max} and H_s during spring – summer (Fig. 7b). Episodically, high peaks in H_s, and especially H_{max}, were noticed outside periods of strong winds, which are likely the result of (primary) ship-induced waves which are particularly frequent in the study area.

Time series of water depths at high tide, h_{max}, measured at SH and SL are shown in Fig. 7d. Mean h_{max} at SH was 0.65 m, reaching a maximum value of 1.97 m on January 13, 2017, while mean h_{max} at SL was 4.14 m, and reaching a maximum value of 5.64 m on that same day. Variation in h_{max} is primarily attributed to the spring–neap tidal constituent although a seasonality is also present. The latter is associated with the inter-annual variability in wind climate, with higher h_{max} resulting from winter storm tides (e.g. January 13, 2017). Similar inter-annual variability in wind climate as well as in freshwater river discharge resulted in a seasonality of tidally-averaged SSC in the nearby estuarine channel (Fig. 7e).

Although long-term seasonal bed level changes recorded at SH and SL (Fig. 7f) seem to coincide with the seasonality in wind climate and associated hydrodynamics (waves and tides), effects of these various forcing factors on the observed short-term (daily) bed level changes are not so discernible at first glance. Daily erosional events during stormy conditions can be indeed identified both at SH and SL, yet other erosional events sometimes of even higher magnitudes occurred during calmer conditions. Accordingly, in the following, we will further investigate potential relationships between daily bed level changes and each of the considered forcing factors.

3.2.2. Correlation analysis

Table 2 shows the results of linear correlations tested between the long-term detrended bed level changes recorded at SH and SL and the corresponding long-term hydrodynamics as well as SSC, as introduced in Fig. 7. We remark that, over the long-term campaign, only daily bed level changes Δz_{t0} and water depth at high tide h_{max} at SL on one hand, and Δz_{t0} and tidally-averaged SSC at SH on the other hand, showed statistically highly significant correlations (p < 0.001; see Table 2). All other paired variables yielded either insignificant (p > 0.05) or significant (p < 0.05) correlations with low scores. Correlation tests based on the original (undetrended) bed level changes did not improve the results (see Table S1). Interestingly, the highly significant correlation observed at SL points to a negative relationship between Δz_{t0} and h_{max} at the low tidal flat, whereby larger water depths are associated with erosion while lower water depths are related to deposition.

In addition to long-term correlations, one may perform correlation tests during periods where external forcing appeared to be particularly significant. Period derived from the wavelet power spectrum where the spring-neap tidal signature was of highest power (see Fig. 6b), resulted

Table 2
Spearman's rank (r_s) correlations between long-term detrended bed level changes Δz_{t0} recorded at the southern high (SH) and low (SL) tidal flat measurement stations and corresponding long-term tidally-maximum and significant wave heights (H_{max} and H_s, respectively), and water depth at high tide h_{max} measured in situ, as well as long-term tidally-averaged SSC measured at the Lillo measurement pole located in the nearby estuarine channel (see Fig. 1). Correlations were based on the full hydrodynamics and SSC records (see Table 1). Statistically significant (p < 0.05) and highly significant (p < 0.001) correlations are underlined and emboldened respectively. *N* indicates the number of observations for every correlation tested.

Variables	SH station		*N*	SL station		*N*
	r_s	p-Value		r_s	p-Value	
(Δz_{t0}, H_{max})	−0.056	0.237	446	−0.014	0.758	475
(Δz_{t0}, H_s)	0.002	0.970	446	<u>−0.110</u>	<u>0.016</u>	<u>475</u>
(Δz_{t0}, h_{max})	<u>−0.121</u>	<u>0.010</u>	<u>446</u>	**−0.430**	**< 0.001**	**475**
(Δz_{t0}, SSC)	**−0.204**	**< 0.001**	**587**	**−0.175**	**< 0.001**	**507**

in correlations between the detrended Δz_{t0} and h_{max} at SL of higher scores and statistical significance ($r_s = -0.47$ with p < 10^{-6} during March – May 2016; $r_s = -0.68$ with p < 10^{-9} during August – September 2016 and $r_s = -0.77$ with p < 10^{-4} during January – February 2017). All highly significant correlations between detrended Δz_{t0} and h_{max} are illustrated in Fig. 8, together with trend lines resulting from corresponding linear regression analyses.

Similarly, correlations between bed level changes and measured wave height parameters were tested both at SH and SL during periods of stormy conditions such as during the 2015–2016 winter season where successive high intensity storms occurred in the study area (see Fig. 7a). Results showed the presence of significant correlations linking original bed level changes and tidally-significant wave heights H_s measured at both tidal flat stations (e.g. $r_s = -0.36$ with p < 0.001 at SL and $r_s = -0.28$ with p = 0.023 at SH from November 2015 to respectively February and January 2016). Correlation tests based on tidally-maximum wave height H_{max} did not yield better results.

Overall, the correlation analysis suggests that, over the long-term, bed level changes at SH and SL do not seem to respond equally to tidal and wave forcing, and that the dominance of one hydrodynamic forcing to another also depends on the considered period. To further assess the relative contribution of tidal and wave forcing on bed level dynamics at the low and high tidal flat, in the following we will focus on the investigation of the hydrodynamic forcing at the intra-tidal time scale.

3.3. Relations of intra-tidal sediment dynamics to hydrodynamic forcing

3.3.1. General time series

Intra-tidal time series of hydrodynamics and turbidity recorded at stations SH and SL during a spring tidal cycle, which was selected within the intensive campaign, are shown in Fig. 9. The presence of a tidal asymmetry can be deduced at both locations as the intra-tidal variation of water levels η describe a fast flood phase followed by a slower ebb phase (Fig. 9a and b).

Fig. 9c and d display the intra-tidal time series of individual wave heights H recorded at SH and SL. We observed the presence of sudden peaks in H at SH, with the same peaks in time also recorded at SL. Peak wave heights recorded at SH and SL for most of them likely correspond to ship-induced waves, as highlighted by the recorded ship passages (green dots). Moreover, recorded waves seem to vary similarly over the tidal cycle at the two locations; wave heights were particularly high at the first and last moments of tidal immersion and decreased as the water depth increased, ultimately reaching a minimum value at high tide.

Time series of wave orbital velocities U_w, current velocities U and turbidity measured at SH and SL are shown in Fig. 9e and f. Intra-tidal variations in U clearly points to a flood dominated tidal asymmetry, typical of shallow water environments. Highest U_w occurred at the beginning and end of the flood and ebb phases respectively, where the wave height to water depth ratio was the highest (see Fig. 9c and d). Turbidity primarily covariates with U_w at SH, reaching its maximum value at the beginning and end of the tidal inundation, whereas variation of turbidity at SL clearly follows U, reaching its maximum value at the moment when peak flood velocity occurred. Periods of high turbidity associated with high U_w also occurred at SL during shallow water depths at the beginning and end of the tidal inundation, yet to a lower magnitude. Intra-tidal hydrodynamics during a neap tidal cycle globally showed similar patterns (Fig. S3), but with a much lower tidal asymmetry. During stormy conditions (Fig. S4), U_w became dominant over U, reaching a maximum value of 1.19 m s^{-1}, and coinciding with a maximum peak of turbidity.

Overall, the visual comparison of the time series of U_w, U and turbidity seem to indicate that wave forcing is more significant than tidal forcing in driving intra-tidal sediment dynamics at SH, whereas the opposite occurs at SL. To confirm this, impacts of tidal and wave forcing will be further examined in the following using parameters relevant for
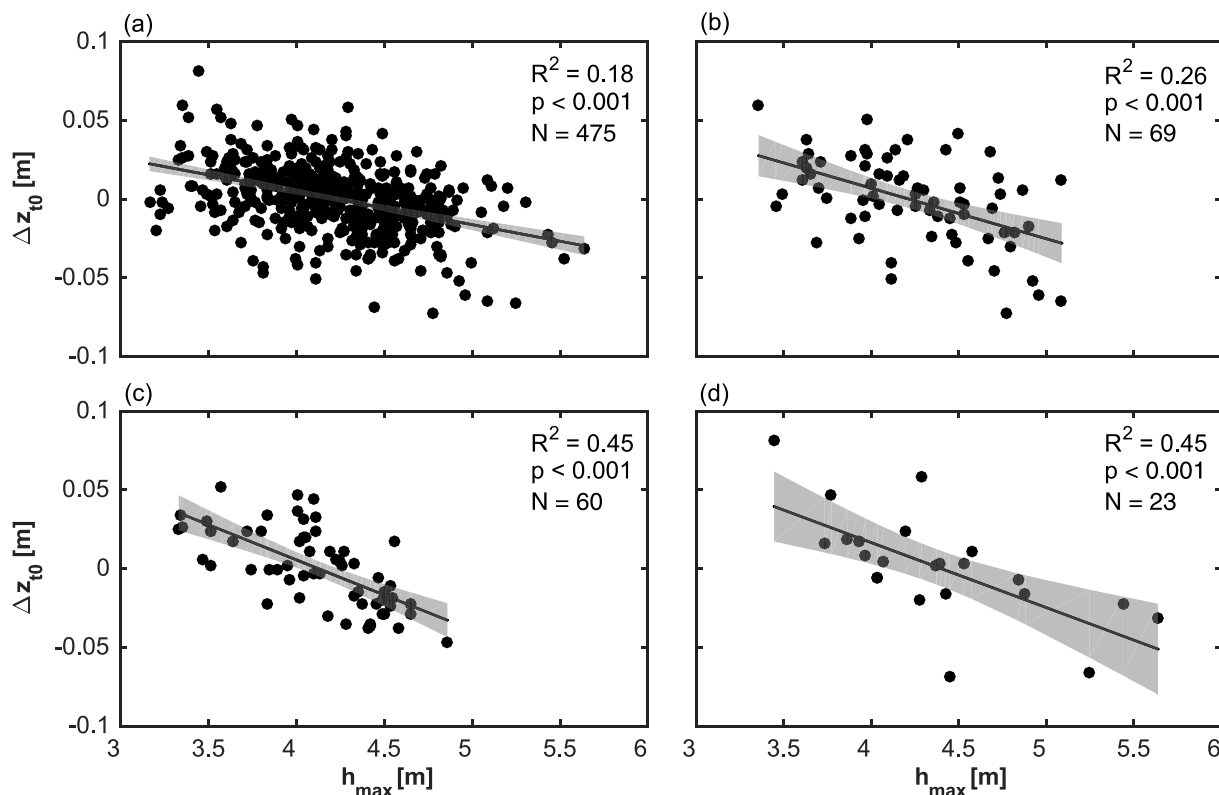
Fig. 8. Scatter plots of detrended bed level changes Δz_{t0} against water depth at high tide h_{max} measured at SL during (a) the entire long-term campaign, (b) March – May 2016, (c) July – September 2016 and (d) January – February 2017. Every scatter plot is supplemented with an Ordinary Least Square (OLS) linear regression model of equation (a) $\Delta z_{t0} = 0.09 - 0.021h_{max}$, (b) $\Delta z_{t0} = 0.135 - 0.032h_{max}$, (c) $\Delta z_{t0} = 0.184 - 0.045h_{max}$ and (d) $\Delta z_{t0} = 0.182 - 0.041h_{max}$. Coefficients of determination R^2, prediction bounds (95%), p-values and number of observations N are also displayed.

assessing bed sediment resuspension and transport.

3.3.2. Wave vs. current-induced hydrodynamic proxies of bed sediment motion

A comparison was performed between tidally-averaged wave-induced bed shear stress $\langle \tau_w \rangle$ and tidally-averaged current-induced bed shear stress $\langle \tau_c \rangle$ estimated at all four measurement stations (Fig. 10), during the intensive campaign.

In analogy with the investigation of wave orbital and current velocity profiles (see Fig. 9e and f), we observe that $\langle \tau_w \rangle$ exceeded $\langle \tau_c \rangle$ at SH and even exceeded the local critical shear stress for sediment motion τ_{cr} during several tidal cycles (Fig. 10b), therefore suggesting a significant wave impact on sediment dynamics during those moments. In contrast $\langle \tau_c \rangle$ was always superior to $\langle \tau_w \rangle$ at SL, except during the storm on November 20, 2016 (see Fig. 10c and d). Additionally, a majority of $\langle \tau_c \rangle$ exceeded the local τ_{cr}, thus denoting a frequent and significant tidal impact on sediment dynamics at SL during the intensive campaign. Sediment resuspension was particularly significant during spring tidal conditions, when all $\langle \tau_{c, spring} \rangle$ values were higher than τ_{cr}, whereas $\langle \tau_{c, neap} \rangle$ rarely exceeded τ_{cr}.

Patterns of wave-induced and current-induced bed shear stress at the tidal flat measurement stations of the northern transect followed those previously described, i.e. $\langle \tau_w \rangle > \langle \tau_c \rangle$ at NH and $\langle \tau_c \rangle > \langle \tau_w \rangle$ at NL (Fig. 10a and c). Nevertheless, at NH $\langle \tau_w \rangle$ barely exceeded τ_{cr}, therefore suggesting an a much lower to insignificant wave impact on sediment dynamics during the intensive campaign.

The comparison of the hydrodynamic shear stresses with the local critical shear stress for sediment motion should be however made with caution here. Indeed, the method used to calculate the latter parameter is only valid for non-cohesive sediments (Soulsby and Whitehouse, 1997). While sediments are sandy at SL, they are primarily muddy at

the three other stations, but characterized by a much higher proportion of silt vs. clay, with d_{50} values corresponding to coarse silt. Therefore, we did not aim to seek precise quantitative predictions, but instead to reveal relative differences in spatial patterns of bed sediment motion in between the different locations, which have shown to conform with the previous results, as will be summarized in the next section.

4. Discussion

Intertidal flats provide valuable ecological functions, such as habitat for specialized benthic animals and plants, carbon sequestration, and shoreline protection (e.g. Paterson et al., 2009; Barbier et al., 2011). Sediment bed level changes ranging from daily to seasonal timescales represent key drivers controlling this ecological functioning (e.g. Bouma et al., 2016; Balke et al., 2011, 2013; Silinski et al., 2016). Nevertheless, studies that combine high-resolution daily measurements and at the same time long-term seasonal data sets on bed level changes in relation to hydrodynamic forcing factors are relatively scarce so far. The present research has revealed that high-resolution daily bed level dynamics in a macrotidal flat showed a seasonal periodicity and shorter-term fortnightly periodicity. The latter was found to be driven by spring-neap tidal forcing. On the other hand, daily bed level changes and intra-tidal sediment resuspension were related to both tidal and wave forcing. Furthermore, our study indicated that the balance between tidal and wave forcing is location dependent, with tidally-dominated sediment dynamics on the low intertidal flat locations and wave dominated sediment dynamics at the high locations. The spatio-temporal patterns of bed level changes and associated hydrodynamic forcing are illustrated in Fig. 11 and will be discussed in detail in the following.
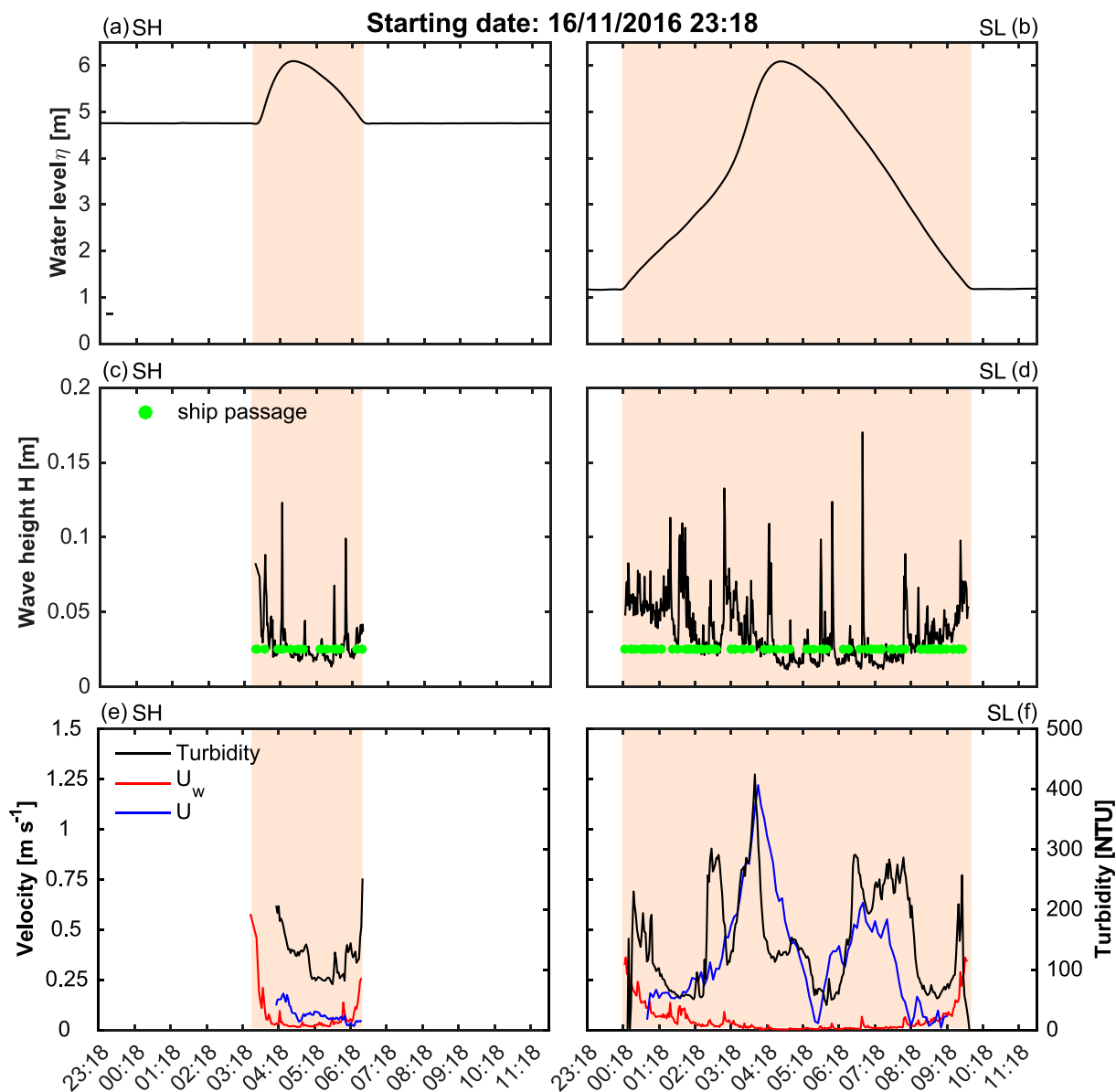
Fig. 9. Temporal evolution of water level η, wave height H, wave orbital velocity U_w current velocity U and turbidity respectively recorded at the (a, c, e) southern high (SH) and (b, d, f) southern low (SL) tidal flat measurement stations during a spring tidal cycle starting on November 16, 2016 23:18:00. Tidally-averaged W_s was 7.0 m s^{-1} and tidally-averaged W_{dir} corresponded to southwesterly winds. For a matter of visualization, recorded η, H, U_w and turbidity were averaged over 2 min at both locations. U measured at SH corresponds to (ADV-derived) point current velocities, also averaged over 2 min, whereas U at SL represents (ADCP-derived) depth-averaged current velocities, kept at the original measurement frequency (i.e. 5 min; see Table 1). Every green dot represents the time of passage of a ship in the S entry line, retrieved using the AIS data. The light beige shaded areas delineate the actual inundation phases at SH and SL during the recorded tidal cycle. (For interpretation of the references to colour in this figure legend, the reader is referred to the web version of this article.)

4.1. Drivers of intra-tidal to daily bed level dynamics

4.1.1. At the low tidal flat

At the low tidal flat, such as at SL, tides clearly represent the dominant driving force of bed level dynamics. As a matter of fact, the low tidal flat, characterized by a low elevation within the tidal frame combined with the macrotidal regime specific to the study area, experiences high tidal inundation depth, duration and frequency (see Figs. 7d and 9b). Such a significant tidal regime generates flood and ebb currents that can attain speeds well above 1 m s^{-1} during spring tides (see Fig. 9f) causing sediment resuspension locally, as manifested by the concomitant peak of turbidity (see Fig. 9f) as well as $\langle \tau_c \rangle$ exceeding τ_{cr} (see Fig. 10d). Sediment resuspension is furthermore facilitated by the non-cohesive nature of the surficial sediments specific to the southern low tidal flat zone (see Figs. 4 and S1). Conversely, during neap tides,

lower peak flood and ebb current velocities occur (see Fig. S3), resulting in $\langle \tau_c \rangle$ rarely exceeding τ_{cr} and hence triggering lower sediment resuspension. These intra-tidal processes that depict a spring–neap variation explain the observed long-term negative linear relationship between water depth and net daily bed level changes (see Fig. 8a) and, by extension, the observed fortnightly periodicity in the net daily bed level changes (see Figs. 5d and 6b). Indeed, peak flood and peak ebb current velocities are related to tidal range (and the proportional water depth) via a positive linear relationship which has been tested and validated in situ during the intensive campaign at NL and SL (see Fig. S5), and which is also well-documented in the literature (e.g. Christie et al., 1999; Bouma et al., 2005; Vanlierde et al., 2014).

However, the impacts of tides alone on bed level dynamics do not appear to be continuously significant over an annual timescale (see Fig. 6b). Episodically occurring waves at SL can generate bottom orbital
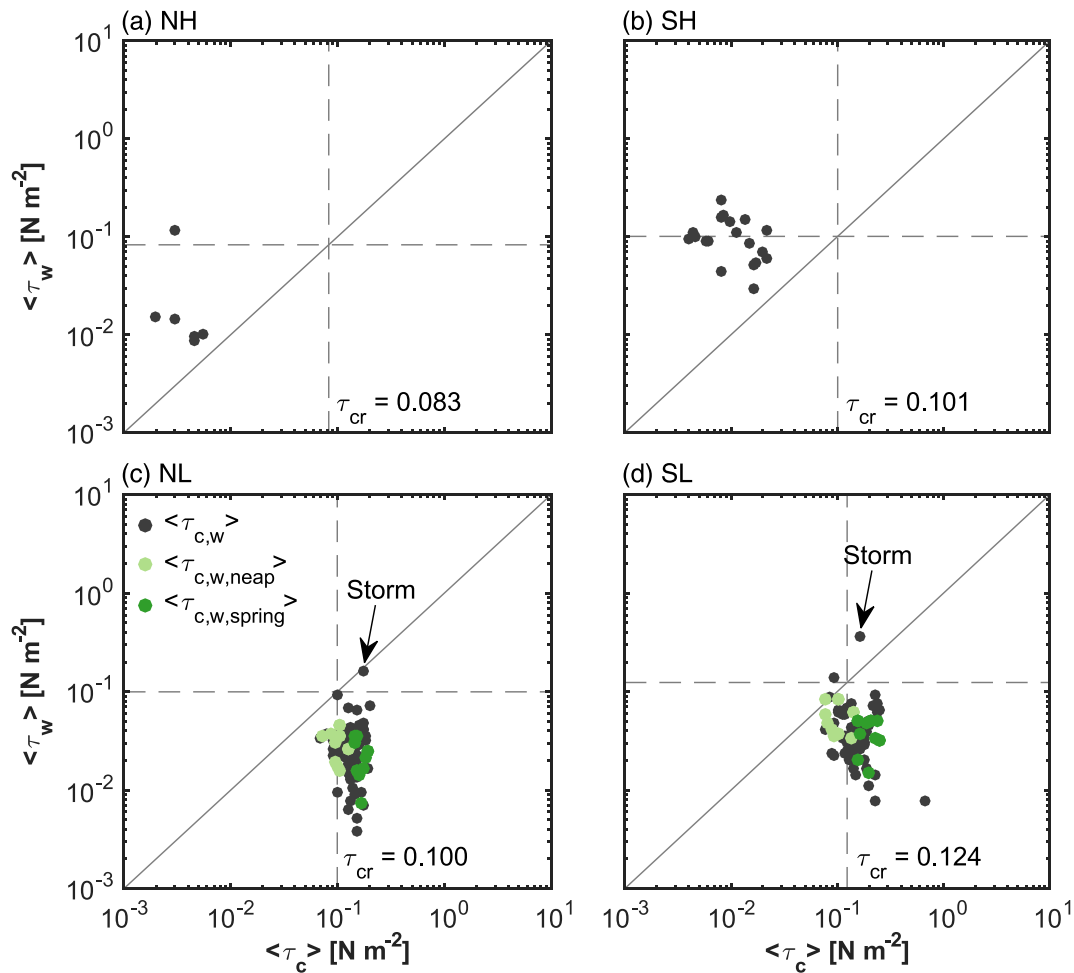
Fig. 10. Scatter plot of tidally-averaged wave-induced bed shear stress $\langle\tau_w\rangle$ vs. tidally-averaged current-induced bed shear stress $\langle\tau_c\rangle$ recorded at the (a) northern high (NH), (b) southern high (SH), (c) northern low (NL) and (d) southern low (SL) tidal flat measurement stations during the intensive campaign (i.e. from October 27, 2016 to December 12, 2016, except for SH where the pressure sensor was repaired and reinstalled on November 09, 2016). Dashed lines with corresponding critical bed shear stress τ_{cr} for sediment motion are displayed for every station considered. $\langle\tau_w\rangle$ and $\langle\tau_c\rangle$ at NL and SL are further differentiated by periods of neap and spring tides.

velocities above $30\,\mathrm{cm\,s^{-1}}$ (see Fig. 9f), and sometimes even higher during stormy conditions, triggering substantial intra-tidal sediment resuspension (Fig. S4) which can lead to net abrupt erosion (see Figs. 3d and 7f). Nevertheless, neither maximum nor significant wave heights did relate to the daily bed level changes over the long-term campaign (see Table 2). Therefore, outside stormy conditions, waves appear to be of secondary importance compared to tides in driving daily bed level changes at the low tidal flat.

Similar patterns in hydrodynamic forcing occur at the low tidal flat of the northern transect, (NL) where tides represent the dominant hydrodynamic forcing. And despite the spring-neap tidal signature on bed level dynamics was less pronounced than at SL, the comparison of $\langle\tau_c\rangle$ with local τ_{cr} (see Fig. 10c) at NL seems also to suggest a certain morphological impact of the tides on bed level dynamics, at least during the intensive campaign. Surficial sediments at NL are predominantly muddy (see Fig. S1) but clay content lies just in the lower range of 5–10%, which is considered as a threshold value between cohesive and non-cohesive sediment behavior (van Ledden et al., 2004), therefore suggesting that sediments at NL do not behave strictly cohesively and may be prone to resuspension by tidal action. Nevertheless, additional measurements of tidal hydrodynamics at NL should be performed to better appraise and conclude on the morphological significance of the tides over the long-term. Indeed the concave-up topographic profile of the northern transect may also carry the signature of past wave activity

(Friedrichs and Aubrey, 1996; Friedrichs, 2011; Waeles et al., 2004; Bearman et al., 2010; Zhou et al., 2015; Hunt et al., 2016).

In the context of macrotidal settings, Deloffre et al. (2005) concluded that tidal forcing was also the dominant driving force responsible for the erosion of a mudflat located in the upper Seine estuary, France. Interestingly, they similarly observed a fortnightly periodicity in the spectral analysis of bed level changes, which was attenuated during periods of high river flow. In contrast with the Seine river, the Scheldt river is characterized by a very low freshwater discharge in such a way that a significant effect of river flow on the attenuation of the fortnightly periodicity in the daily bed level changes at the Galgeschoor is quite unlikely. Hu et al. (2017) noticed a similar spatial distribution of τ_c in the mesotidal Westerschelde, Netherlands (~30 km downstream of the Galgeschoor), where higher τ_c, denoting a significant tidal forcing, were found in the low zone of two contrasting wave exposed, but flatter and wider tidal flats. Yet, results here show that the impact of tidal forcing can be occasionally hindered by stronger wave impacts induced by more windy or stormy weather, such as during the late 2015 – early 2016 winter season.

4.1.2. At the high tidal flat

At the high tidal flat, such as at SH, waves become the dominant driving force of bed level dynamics, especially at the intra-tidal time scale. Indeed, the high tidal flat, characterized by a high elevation
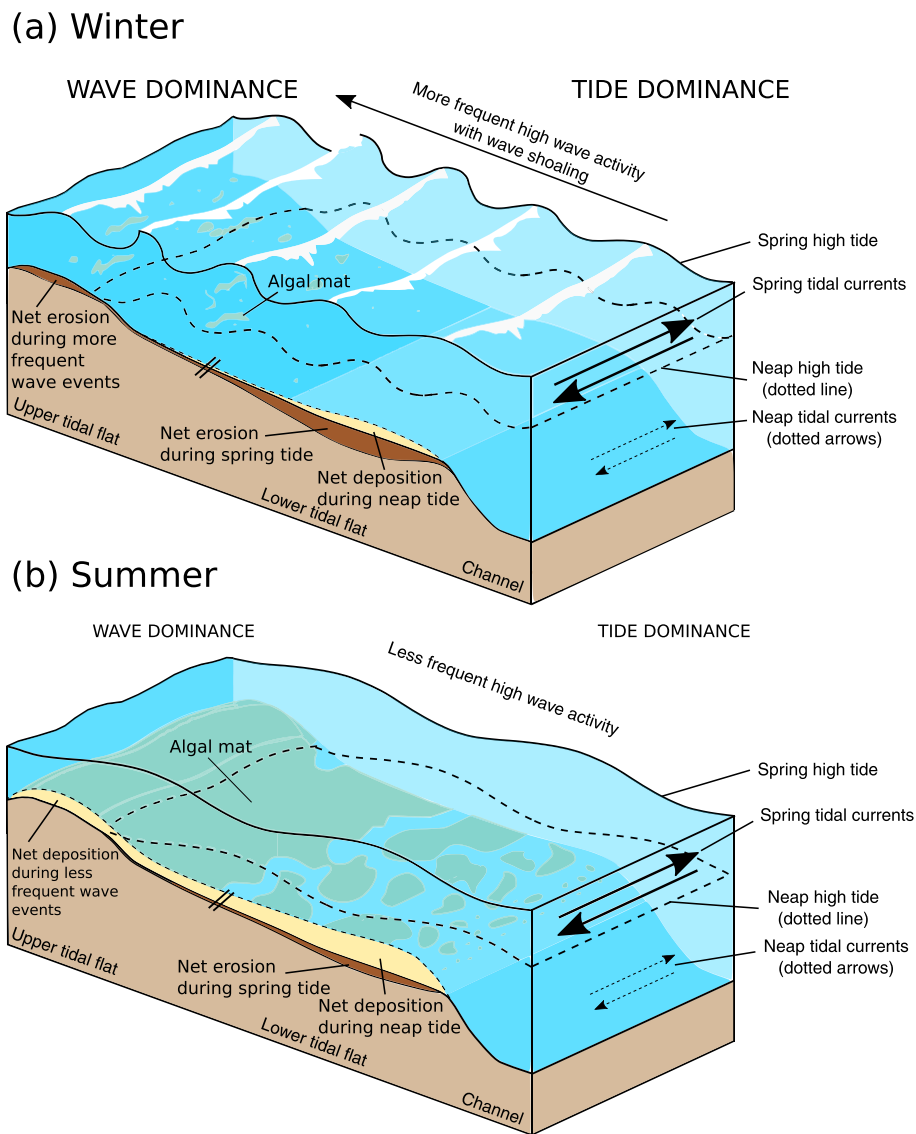
Fig. 11. Conceptual model for the morphodynamic response of the tidal flat of Galgeschoor due to tidal and wave actions during (a) winter and (b) summer. The depicted processes here may be applicable to other narrow fringing tidal flats located in the inner sections of macrotidal estuaries.

within the tidal frame near the level of the mean high water level (see Fig. 2), experiences little tidal inundation depth, duration and frequency. This generates weaker flood and ebb currents (see Fig. 9e) which, in combination with the more cohesive nature of the surficial sediments of the high tidal flat zone (see Fig. 4), do not trigger sediment resuspension locally, even during spring tides. In contrast, higher waves occur at the high tidal flat, as indicated by the higher significant wave heights recorded at SH during the long-term campaign (see Fig. 7c), and particularly under the weaker, more frequent daily winds (see Fig. S6). These higher waves primarily result from shoaling effects, as manifested by the higher wave steepness observed at the high tidal flat (see Fig. S7). These higher waves generate significant orbital velocities which, in combination with the shallower water depth conditions of the high tidal flat, can reach more easily the bottom, eventually causing sediment resuspension during the first and last moments of tidal immersion, as illustrated by the concomitant turbidity peaks (see Fig. 9e). In line with these observations, several recorded tidal cycles during the intensive campaign showed that $\langle \tau_w \rangle$ exceeded the local τ_{cr} at SH, being one order of magnitude higher than $\langle \tau_c \rangle$ (see Fig. 10b).

Nevertheless, our results also show that wave height parameters did not correlate well to the net daily bed level changes at SH (as well as SL)

over the long-term campaign (see Table 2). One possible reason may be related to the differences in measurement frequencies between the instruments used to measure the variables of interest (see Table 1). Pressure sensors provided high-resolution (instantaneous) wave records. However, SED sensors provided records of net bed level changes between tidal cycles when the tidal flat was emerged and during daytime (~daily measurement frequency). Net daily bed level changes may be significantly lower than the magnitudes of the gross erosion and deposition within a tidal cycle, as also documented in the literature (Andersen et al., 2005; Shi et al., 2014; Zhu et al., 2014), thus complicating a direct comparison with the corresponding wave forcing.

Similarly, the wave forcing also predominates in the high tidal flat of the northern transect (NH), which is notably illustrated by the observed higher $\langle \tau_w \rangle$ than $\langle \tau_c \rangle$ during the intensive campaign (see Fig. 10a). However, unlike at SH, $\langle \tau_w \rangle$ rarely exceeded the local τ_{cr}, indicating that the waves were not significant in driving bed level dynamics, as also suggested by the limited bed level changes observed at NH over the long-term (see Fig. 3a). This wave morphological insignificance at that particular location may be explained by the finer and more cohesive surficial sediments observed at NH which contribute to a higher shear strength of the sediment surface locally.

A few studies have previously pointed out the dominance of wave forcing in driving short-term sediment dynamics in shallower intertidal areas, even in macrotidal settings (e.g. Weir and McManus, 1987; Christie et al., 1999; Verney et al., 2007). Within the Scheldt estuary, Hu et al., 2017 showed that the long-term daily bed level changes, recorded in the two contrasting wave exposed tidal flats in the Westerschelde, were only significantly correlated with τ_w at the exposed site, regardless of the location on the actual flat. Our results showed that wave forcing can be morphologically significant in the upper intertidal zone even in sheltered sites (fetch length < 2 km).

4.2. Drivers of seasonal bed level dynamics

In addition to intra-tidal and daily bed level dynamics, seasonal bed level dynamics has also been observed at the two stations of the southern transect (see Fig. 3b and d). This seasonality of the bed level changes is most likely related to the seasonality of the hydrodynamics, as already pointed out (see Fig. 7), alongside with benthic biology (Widdows et al., 2000). In essence, more windy weather and associated higher waves favor erosion during winter. This tendency is further amplified by the lower bed stabilization provided by the microphytobenthos, as reduced solar radiation and temperature typically limit biological growth in winter (Andersen et al., 2006). In contrast, calmer weather in summer favors the tendency for net deposition which, combined with higher solar radiation and temperature, increase microphytobenthos productivity, with the effect of stabilizing the sediment bed. Indeed, the microphytobenthos secretes adhesive polymers (EPSs), which together form biofilms that in turn increase sediment cohesion (Van Colen et al., 2014). The field campaign did not involve long-term measurements of (micro)phytobenthos productivity at the Galgeschoor, yet the visual comparison of a sequence of photos of the SEB plot at SH taken during the monthly field visits seems to support the presence of a seasonality in benthic biology (Fig. S8). In particular, an algal mat of *Vaucheria* progressively grew on top of the sediment surface starting from May 2016 to late autumn where it disappeared again. This seasonal variation approximately coincides with the corresponding seasonal pattern of bed level changes observed at SH (see Fig. 3b). Likewise, a benthic diatom film was also observed at SH, particularly during the spring and summer months (see Fig. S8c).

This relationship between seasonal bed level dynamics and seasonal wave climate and benthic biology is consistent with a series of qualitative and quantitative findings from previous studies conducted in other NW European estuaries in all tidal regimes, such as the microtidal Rømø Bight, Denmark (Andersen et al., 2005, 2006) and the mesotidal Deben estuary, UK (Frostick and McCave, 1979), Ardmillan Bay, Ireland (Kirby et al., 1993), and Dollard estuary, Netherlands (Dyer et al., 2000b).

4.3. Implications for the formation of intertidal sediment deposits

In view of the spatial distribution of the tidal vs. wave dominance controlling contemporary sediment dynamics across the studied tidal flat, one may expect that ancient intertidal sediment deposits and sedimentary records may also reflect this spatial variability. Accordingly, sedimentary structures typical of intertidal flats of inner macrotidal estuaries and formed under the influence of tidal currents may be indicative of a sedimentary facies of low intertidal flats with predominantly deep water conditions (e.g. ~4 m deep at high tide at Galgeschoor). Sedimentary structures indicative for this sedimentary facies comprise current-generated ripples, whose geometries are particularly preserved with increasing bed slopes, and beddings such as flaser, wavy and lenticular beddings (Dalrymple et al., 1990, 1991). The latter internal sedimentary structures materialize a sequence from muddy sand to sandy and slightly sandy mud facies (Reineck and Wunderlich, 1968; Daidu et al., 2013) and so are profusely found in mixed sand mud flats and are usually well-preserved in the sedimentary

record (Davis Jr, 2012).

On the other hand, sedimentary structures of inner estuarine intertidal flats and formed by waves may be indicative of a sedimentary facies of high intertidal flats with predominantly shallow water conditions (e.g. < 1 m deep at high tide at Galgeschoor). Typical surface sedimentary structures in this settings may include bedforms such as wave-generated ripples, sometimes dissected by narrow streams of current ripples (Flemming, 2012). Tidal rhythmites and other subsurface sedimentary structures that develop within this sedimentary facies and are tidal signatures are typically less preserved in the sedimentary record due to wave action (Davis Jr, 2012).

5. Conclusions

The present research has intended to bring further insights into short-term sediment dynamics, ranging from intra-tidal to daily and seasonal timescales, which greatly control the ecogeomorphic functioning of intertidal flats. To this purpose, a high-resolution data set of bed level changes and hydrodynamic forcing spanning a period of more than a year was collected in a narrow fringing macrotidal flat. Results revealed that daily bed level dynamics showed a seasonal trend governed by the seasonality of wind and wave climates and benthic biology, and a shorter-term fortnightly periodicity driven by spring-neap tidal forcing. At even shorter timescales, daily bed level changes and intra-tidal sediment resuspension were related to either tidal or wave forcing, depending on the location within the intertidal zone. This complex spatio-temporal variability in bed level changes and the associated hydrodynamic forcing highlight the importance of conducting comprehensive and detailed field measurements to study sediment dynamics in intertidal environments.

Appendix A. Supplementary data

Supplementary data to this article can be found online at https://doi.org/10.1016/j.margeo.2019.03.001.

References

Amos, C.L., 1995. Siliclastic tidal flats. In: Perillo, G.M.E. (Ed.), Geomorphology and Sedimentology of Estuaries. Elsevier, Amsterdam, pp. 273–306.

Andersen, T., Lund-Hansen, L., Pejrup, M., Jensen, K., Mouritsen, K., 2005. Biologically induced differences in erodibility and aggregation of subtidal and intertidal sediments: a possible cause for seasonal changes in sediment deposition. J. Mar. Syst. 55, 123–138. https://doi.org/10.1016/j.jmarsys.2004.09.004.

Andersen, T., Pejrup, M., Nielsen, A., 2006. Long-term and high-resolution measurements of bed level changes in a temperate, microtidal coastal lagoon. Mar. Geol. 226, 115–125. https://doi.org/10.1016/j.margeo.2005.09.016.

Anderson, T.W., Darling, D.A., 1952. Asymptotic theory of certain "goodness of fit" criteria based on stochastic processes. Ann. Math. Stat. 23, 193–212.

Balke, T., Bouma, T.J., Horstman, E., Webb, E., Erftemeijer, P., Herman, P., 2011. Windows of opportunity: thresholds to mangrove seedling establishment on tidal flats. Mar. Ecol. Prog. Ser. 440, 1–9. https://doi.org/10.3354/meps09364.

Balke, T., Bouma, T.J., Herman, P.M., Hortman, E., Sudtongkong, C., Webb, E., 2013. Cross-shore gradients of physical disturbance in mangroves: implications for seedling establishment. Biogeosciences 10, 5411–5419. https://doi.org/10.5194/bg-10-5411-2013.

Barbier, E.B., Hacker, S.D., Kennedy, C., Koch, E.W., Stier, A.C., Silliman, B.R., 2011. The value of estuarine and coastal ecosystem services. Ecol. Monogr. 81, 169–193. https://doi.org/10.1890/10-1510.1.

Bearman, J.A., Friedrichs, C.T., Jaffe, B.E., Foxgrover, A.C., 2010. Spatial trends in tidal at shape and associated environmental parameters in South San Francisco Bay. J.

Coast. Res. 26, 342–349. https://doi.org/10.2112/08-1094.1.

Bouma, T.J., Vries, M.B.D., Low, E., Kusters, L., Herman, P.M.J., Tánczos, I.C., Temmerman, S., Hesselink, A., Meire, P., van Regenmortel, S., 2005. Flow hydrodynamics on a mudflat and in salt marsh vegetation: identifying general relationships for habitat characterisations. Hydrobiologia 540, 259–274. https://doi.org/10.1007/s10750-004-7149-0.

Bouma, T.J., van Belzen, J., Balke, T., van Dalen, J., Klaassen, P., Hartog, A.M., Callaghan, D.P., Hu, Z., Stive, M.J.F., Temmerman, S., Herman, P.M.J., 2016. Short-term mudflat dynamics drive long-term cyclic salt marsh dynamics. Limnol. Oceanogr. 61, 2261–2275. https://doi.org/10.1002/lno.10374.

Carniello, L., Defina, A., D'Alpaos, L., 2009. Morphological evolution of the Venice lagoon: evidence from the past and trend for the future. J. Geophys. Res. Earth Surf. 114. https://doi.org/10.1029/2008JF001157.

Christiansen, C., Vlund, G., Lund-Hansen, L.C., Bartholdy, J., 2006. Wind influence on tidal at sediment dynamics: field investigations in the Ho Bugt, Danish Wadden Sea. Mar. Geol. 235, 75–86. https://doi.org/10.1016/j.margeo.2006.10.006.

Christie, M.C., Dyer, K.R., Turner, P., 1999. Sediment flux and bed level measurements from a macro tidal mudflat. Estuar. Coast. Shelf Sci. 49, 667–688. https://doi.org/10.1006/ecss.1999.0525.

Daidu, F., Yuan, W., Min, L., 2013. Classifications, sedimentary features and facies associations of tidal flats. J. Palaeogeogr. 2, 66–80.

Dalrymple, R.W., Knight, R.J., Zaitlin, B.A., Middleton, G.V., 1990. Dynamics and facies model of a macrotidal sand-bar complex, Cobequid Bay—Salmon River Estuary (Bay of Fundy). Sedimentology 37, 577–612. https://doi.org/10.1111/j.1365-3091.1990.tb00624.x.

Dalrymple, R.W., Makino, Y., Zaitlin, B.A., 1991. Temporal and spatial patterns of rhythmite deposition on mudflats in the macrotidal, Cobequid Bay-Salmon River estuary, Bay of Fundy, Canada. In: Smith, D.G., Reinson, G.E., Zaitlin, B.A., Rahmani, R.A. (Eds.), Clastic tidal sedimentology. Can Soc Petrol Geol Mem 16. pp. 137–160.

Davis Jr., R.A., 2012. Tidal signatures and their preservation potential in stratigraphic sequences. In: Davis Jr.R., Dalrymple, R. (Eds.), Principles of Tidal Sedimentology. Springer, Dordrecht.

Deloffre, J., Laffite, R., Lesueur, P., Lesourd, S., Verney, R., Guzennec, L., 2005. Sedimentary processes on an intertidal mudflat in the upper macrotidal Seine estuary, France. Estuarine, Coastal and Shelf Science 64, 710–720.doi:https://doi.org/10.1016/j.ecss.2005.04.004.

Dyer, K.R., Christie, M.C., Wright, E.W., 2000a. The classification of intertidal mudflats. Cont. Shelf Res. 20, 1039–1060.

Dyer, K.R., Christie, M.C., Feates, N., Fennessy, M.J., Pejrup, M., van der Lee, W., 2000b. An Investigation into processes influencing the morphodynamics of an intertidal mudflat, the Dollard Estuary, The Netherlands: I. Hydrodynamics and suspended sediment. Estuar. Coast. Shelf Sci. 50, 607–625. https://doi.org/10.1006/ecss.1999.0596.

Flemming, B.W., 2012. Siliciclastic back-barrier tidal flats. In: Davis Jr.R.A., Dalrymple, R.W. (Eds.), Principles of Tidal Sedimentology. Springer, Dordrecht.

Fredsøe, J., Deigaard, R., 1992. Mechanics of Coastal Sediment Transport. Advanced Series on Ocean Engineering 3 World Scientific Publishing.

Friedrichs, C.T., 2011. Tidal flat morphodynamics: a synthesis, in: De., H.J., We., F.B. (Eds.), Treatise on Estuarine and Coastal Science. Elsevier, Virginia Institute of Marine Science: Gloucester POint, VA, USA. volume 3, pp. 137–170.

Friedrichs, C.T., Aubrey, D.G., 1996. Uniform Bottom Shear Stress and Equilibrium Hyposometry of Intertidal Flats. American Geophysical Union (AGU). chapter 24. pp. 405–429. doi:https://doi.org/10.1029/CE050p0405.

Frostick, L.E., McCave, I.N., 1979. Seasonal shifts of sediment within an estuary mediated by algal growth. Estuar. Coast. Mar. Sci. 9, 569–576. https://doi.org/10.1016/0302-3524(79)90080-X.

Gao, S., 2009. Geomorphology and sedimentology of tidal flats. In: Perillo, G.M.E., Wolanski, E., Cahoon, D.R., Brinson, M.M. (Eds.), Coastal Wetlands: An Integrated Ecosystem Approach. Elsevier, Amsterdam, pp. 295–316.

Green, M.O., Coco, G., 2014. Review of wave-driven sediment resuspension and transport in estuaries. Rev. Geophys. 52, 77–117. https://doi.org/10.1002/2013RG000437.

Hu, Z., Lenting, W., van der Wal, D., Bouma, T.J., 2015. Continuous monitoring bed-level dynamics on an intertidal at: introducing novel, stand-alone high-resolution sed-sensors. Geomorphology 245, 223–230. https://doi.org/10.1016/j.geomorph.2015.05.027.

Hu, Z., Yao, P., van der Wal, D., Bouma, T.J., 2017. Patterns and drivers of daily bed-level dynamics on two tidal flats with contrasting wave exposure. Sci. Rep. 7, 7088.

Hunt, S., Bryan, K.R., Mullarney, J.C., Pritchard, M., 2016. Observations of asymmetry in contrasting wave- and tidally-dominated environments within a mesotidal basin: implications for estuarine morphological change. Earth Surf. Process. Landf. 41, 2207–2222. https://doi.org/10.1002/esp.3985. eSP-15-0287.R1.

Kirby, R., Bleakley, R.J., Weatherup, S.T.C., Raven, P.J., Donaldson, N.D., 1993. Effect of episodic events on tidal flat stability, Ardmillan Bay, Strangford Lough, Northern Ireland, p. 378–392. In: Mehta, A.J. (Ed.), Nearshore and Estuarine Cohesive Sediment Transport. American Geophysical Union, Washington, D.C..

le Hir, P., Roberts, W., Cazaillet, O., Christie, M.C., Bassoullet, P., Bacher, C., 2000. Characterization of intertidal flat hydrodynamics. Cont. Shelf Res. 20 (12/13), 1433–1459.

Lee, H.J., Jo, H.R., Chu, Y.S., Bahk, K.S., 2004. Sediment transport on macrotidal flats in Garolim Bay, west coast of Korea: significance of wind waves and asymmetry of tidal currents. Cont. Shelf Res. 24, 821–832. https://doi.org/10.1016/j.csr.2004.01.005.

Maris, T., Meire, P., 2016. OMES rapport 2015. Onderzoek naar de gevolgen van het Sigmaplan, baggeractiviteiten en havenuitbreiding in de Zeeschelde op het milieu. Technical Report. University of Antwerp. 172.

Möller, I., Kudella, M., Rupprecht, F., Spencer, T., Paul, M., Van Wesenbeeck, B.K., Wolters, G., Jensen, K., Bouma, T.J., Miranda-Lange, M., et al., 2014. Wave attenuation over coastal salt marshes under storm surge conditions. Nat. Geosci. 7, 727. https://doi.org/10.1038/ngeo2251.

Nolte, S., Koppenaal, E.C., Esselink, P., Dijkema, K.S., Schuerch, M., De Groot, A.V., Bakker, J.P., Temmerman, S., 2013. Measuring sedimentation in tidal marshes: a review on methods and their applicability in biogeomorphological studies. J. Coast. Conserv. 17, 301–325. https://doi.org/10.1007/ s11852-013-0238-3.

O'Brien, D.J., Whitehouse, R.J.S., Cramp, A., 2000. The cyclic development of a macro-tidal mudflat on varying timescales. Cont. Shelf Res. 20, 1593–1619. https://doi.org/10.1016/S0278-4343(00)00039-X.

Paterson, D.M., Aspden, R., Black, K., 2009. Intertidal ats: ecosystem functioning of soft sediment systems. In: Perillo, G., Wolanski, E., Cahoon, D., Brinson, M. (Eds.), Coastal Wetlands: An Integrated Ecosystem Approach. Elsevier, Netherlands, pp. 317–338.

Pethick, J.S., 1996. The geomorphology of mudflats. In: Nordstrom, K.R., Roman, C.T. (Eds.), Estuarine Shores: Evolution. Environments and Human Alterations Wiley, Chichester, pp. 185–211.

Press, W.H., Teukolsky, S.A., Vetterling, W.T., Flannery, B.P., 1992. Numerical Recipes in FORTRAN (2nd ed.): the Art of Scientific Computing. Cambridge University Press, New York, NY, USA.

Reineck, H.-E., Wunderlich, F., 1968. Classification and origin of flaser and lenticular bedding. Sedimentology 11, 99–104.

Scargle, J.D., 1982. Studies in astronomical time series analysis. II – statistical aspects of spectral analysis of unevenly spaced data. Astrophys. J. 263, 835–853. https://doi.org/10.1086/160554.

Shi, B.W., Yang, S.L., Wang, Y.P., Yu, Q., Li, M.L., 2014. Intratidal erosion and deposition rates inferred from field observations of hydrodynamic and sedimentary processes: A case study of a mudflat—saltmarsh transition at the Yangtze delta front. Continental Shelf Research 90, 109–116. doi:https://doi.org/10.1016/j.csr.2014.01.019.

Silinski, A., van Belzen, J., Fransen, E., Bouma, T.J., Troch, P., Meire, P., Temmerman, S., 2016. Quantifying critical conditions for seaward expansion of tidal marshes: a transplantation experiment. Estuar. Coast. Shelf Sci. 169, 227–237. https://doi.org/10.1016/j.ecss.2015.12.012.

Soulsby, R.L., Whitehouse, R.J.S., 1997. Threshold of sediment motion in coastal environments, in: Pacific Coasts and Ports '97: Proceedings of the 13th Australasian Coastal and Ocean Engineering Conference and the 6th Australasian Port and Harbour Conference. Centre for Advanced Engineering, University of Canterbury, Christchurch, NZ.

Temmerman, S., Meire, P., Bouma, T.J., Herman, P.M., Ysebaert, T., De Vriend, H.J., 2013. Ecosystem-based coastal defence in the face of global change. Nature 504, 79. https://doi.org/10.1038/nature12859.

Van Colen, C., Underwood, G.J.C., Serôdio, J., Paterson, D.M., 2014. Ecology of intertidal microbial biofilms: mechanisms, patterns and future research needs. J. Sea Res. 92, 2–5. https://doi.org/10.1016/j.seares.2014.07.003.

van Ledden, M., Wang, Z.-B., Winterwerp, H., de Vriend, H., 2004. Sand–mud morpho-dynamics in a short tidal basin. Ocean Dyn. 54, 385. https://doi.org/10.1007/s10236-003-0050-y.

Vanlierde, E., Michielsen, S., Vereycken, K., Hertoghs, R., Meire, D., Deschamps, M., Verwaest, T., Mostaert, F., 2011. Onderzoek naar de invloedsfactoren van golfbelasting en de morfologische effecten op slikken en schorren in de Beneden Zeeschelde, meer specifiek op het Galgeschoor: Deelrapport 2: Verslag testmeting van 29/11/2010 - 01/12/2010. Technical Report. Waterbouwkundig Laboratorium & INBO: Antwerpen, België. Versie 4 0. WL Rapporten, 837 03.

Vanlierde, E., Michielsen, S., Vereycken, K., Hertoghs, R., Meire, D., Deschamps, M., Verwaest, T., Mostaert, F., 2014. Tienjarig overzicht van de tijwaarnemingen in het Zeescheldebekken: decennium 2001–2010. Technical Report. Waterbouwkundig Laboratorium: Antwerpen. Versie 5 0. WL Rapporten, 12 071.

Verney, R., Deloffre, J., Brun-Cottan, J.C., Laffite, R., 2007. The effect of wave-induced turbulence on intertidal mudflats: impact of boat traffic and wind. Cont. Shelf Res. 27, 594–612. https://doi.org/10.1016/j.csr.2006.10.005.

Waeles, B., Le Hir, P., Silva Jacinto, R., 2004. Modélisation morphodynamique cross-shore d'un estran vaseux. Compt. Rendus Geosci. 336, 1025–1033.

Wang, C., Temmerman, S., 2013. Does biogeomorphic feedback lead to abrupt shifts between alternative landscape states?: an empirical study on intertidal flats and marshes. J. Geophys. Res. Earth Surf. 118, 229–240. https://doi.org/10.1029/2012JF002474.

Weir, D.J., McManus, J., 1987. The role of wind in generating turbidity maxima in the Tay Estuary. Continental Shelf Research 7, 1315–1318. doi:10.1016/0278-4343(87)90035-5. Dynamics of Turbid Coastal Environments.

Widdows, J., Brinsley, M.D., Salkeld, P.N., Lucas, C.H., 2000. Influence of biota on spatial and temporal variation in sediment erodability and material flux on a tidal at (Westerschelde, The Netherlands). Mar. Ecol. Prog. Ser. 194, 23–37.

Willemsen, P., Borsje, B.W., Hulscher, S.J.M.H., Van der Wal, D., Zhu, Z., Oteman, B., Evans, B., Möller, I., Bouma, T.J., 2018. Quantifying bed level change at the transition of tidal flat and salt marsh: can we understand the lateral location of the marsh edge? J. Geophys. Res. Earth Surf. 123, 2509–2524. https://doi.org/10.1029/2018JF004742.

Yang, S.L., Friedrichs, C.T., Shi, Z., Ding, P-X., Zhu, J., Zhao, Q-Y., 2003. Morphological response of tidal marshes, flats and channels of the Outer Yangtze river mouth to a major storm. Estuaries 26, 1416–1425.doi:https://doi.org/10.1007/BF02803650.

Zhou, Z., Coco, G., van der Wegen, M., Gong, Z., Zhang, C., Townend, I., 2015. Modeling sorting dynamics of cohesive and non-cohesive sediments on intertidal flats under the effect of tides and wind waves. Cont. Shelf Res. 104, 76–91. https://doi.org/10.1016/j.csr.2015.05.010.

Zhu, Q., Yang, S., Ma, Y., 2014. Intra-tidal sedimentary processes associated with combined wave-current action on an exposed, erosional mudflat, southeastern Yangtze River Delta, China. Mar. Geol. 347, 95–106. https://doi.org/10.1016/j.margeo.2013.11.005.